Shallow Water Tidal Currents in Close Proximity to the Seafloor and Boundary-Induced Turbulence

I. Lozovatsky[a], Zhiyu Liu[b, c,*], H.J.S. Fernando[a], J. Armengol[d], and E. Roget[d]

[a] Environmental Fluid Dynamics Laboratories, Departments of Civil Engineering & Geological Sciences, University of Notre Dame, Notre Dame, IN, 46556, USA

[b] State Key Laboratory of Marine Environmental Science, College of Oceanography and Environmental Science, Xiamen University, 422 Siming South Road, Xiamen 361005, China

[c] Physical Oceanography Laboratory, College of Physical and Environmental Oceanography, Ocean University of China, 238 Songling Road, Qingdao 266100, China

[d] Environmental Physics Group, Department of Physics, University of Girona, Girona, E-17071, Catalonia, Spain

Submitted: March 1, 2011

Revised: May 26, 2011

[*] *Corresponding author*: Dr. Zhiyu Liu, State Key Laboratory of Marine Environmental Science, Xiamen University, 422 Siming South Road, Xiamen 361005, China. E-mail: zyliu@xmu.edu.cn

Abstract

ADCP velocity measurements with vertical resolution 0.02 m were conducted in the lowest 0.5 m of the water column at a test site in the western part of the East China Sea to investigate the applicability of the law-of-the-wall very near to the seafloor. The friction velocity u_* and the turbulent kinetic energy dissipation rate $\varepsilon_{wl}(\zeta)$ profiles were calculated using log-layer fits; ζ is the height above the bottom. During a semidiurnal tidal cycle, u_* was found to vary in the range (1–7)×10^{-3} m/s. The law-of-the-wall dissipation profiles $\varepsilon_{wl}(\zeta)$ were consistent with the dissipation profiles $\varepsilon_{mc}(\zeta)$ evaluated using independent microstructure measurements of small-scale shear, except in the presence of westward currents. It was hypothesized that an isolated bathymetric rise (25 m height at a 50 m seafloor) located to the east of the measurement site, is responsible for the latter. Calculation of the depth integrated internal-tide generating body force in the region showed that the flanks of the rise are hotspots of internal-wave energy that may locally produce a significant turbulent zone while emitting tidal and nonlinear internal waves. This distant topographic source of turbulence may enhance the microstructure-based dissipation levels $\varepsilon_{mc}(\zeta)$ in the bottom boundary layer (BBL) beyond the dissipation $\varepsilon_{wl}(\zeta)$ due to purely locally generated turbulence by skin currents. Semi-empirical estimates for dissipation at a distance from the bathymetric rise agree well with the BBL values of ε_{mc} measured 15 km upslope.

1. Introduction

Substantial progress has been achieved recently in studying currents and turbulence in coastal marine bottom boundary layers (BBL) as a result of the development of high-frequency and high vertical resolution acoustic Doppler current profilers (ADCPs) as well as commercial microstructure instruments such as MSS (Prandke and Stips 1998) and Turbomap (Wolk et al. 2002). The profiling of currents in coastal oceans is mainly conducted using upward-looking, bottom-mounted ADCPs, whereas high frequency temporal variations of velocity components at a specific height above the bottom can be obtained by acoustic Doppler velocimeters (ADVs). Field studies on BBL dynamics in shallow waters (Lueck and Lu 1997; Foster et al. 2000; Elliott 2002; Howarth and Souza 2005; Lozovatsky et al. 2008a,b; Liu, Wu et al. 2009) have confirmed the general applicability of log-layer approximation to the velocity profiles $U(\zeta)=\left[u^2(\zeta)+v^2(\zeta)\right]^{1/2}$ in a well-mixed BBL, and therefore the possibility of law-of-the-wall dissipation estimation $\varepsilon_{wl}(\zeta)=c\,u_*^3/\kappa\zeta$ for near-bottom turbulence. Here u and v are horizontal components of the velocity vector, u_* the friction velocity, $\kappa\approx 0.4$ the von Karman constant, c a nondimensional constant of order to unity, and ζ the height above the seafloor. It was found, however, that in the presence of weak stable stratification velocity profile may exhibit a seemingly logarithmic structure, even though this log-layer may not support a constant vertical momentum flux, and u_* so deduced can be much larger than the actual friction velocity. Specific modifications to u_* obtained from shear profiles $dU(\zeta)/d\zeta$ have been suggested (e.g., Friedrichs and Wright 1997; Perlin et al. 2005; Taylor and Sarkar 2008) to account for the

influence of stratification. The u_* deduced from the modified formulae was approximately half of its law-of-the-wall based counterpart.

In non-stationary boundary currents, such as reversing tidal flows, u_* can be considered as constant for relatively short periods, during which the law-of-the-wall is assumed to be valid. If the tidal vector rotates, tracing a circle or slightly stretched ellipse, the friction velocity u_* can remain approximately constant (proportional to the mean velocity magnitude *U*) during the entire tidal cycle. Lozovatsky et al. (2008b) found, however, that the log-layer estimates of u_* in a rotating tidal flow are about twice as much as the u_* calculated via direct eddy correlations $\langle u'w' \rangle$ and $\langle v'w' \rangle$. The difference was attributed to the failure of the log-layer model in relatively thick (~ 10 m) boundary layers of rotating tidal flows. This together with weak stratification effects may lead to erroneously high u_* values compared to those deduced from the eddy correlation technique (Lueck and Lu 1997; Elliott 2002; Lozovatsky et al. 2008a,b). Nevertheless, one can expect that velocity profiles in close proximity to the seafloor ($\zeta < 1$ meter above bottom, mab) are unaffected by stratification and therefore exhibit a canonical log-layer, but data to check this assumption were unavailable until recently. In the summer of 2006, oceanographers of the Ocean University of China (OUC) conducted ADCP measurements in the coastal zone of the East China Sea (ECS) starting from $\zeta = 0.04$ mab up to $\zeta = 0.48$ mab with a vertical resolution of 0.02 m. These data allowed analysis of detailed velocity structure in a rotating tidal flow and evaluation of u_* based on logarithmic velocity profiles (when exist) in the absence of stratification. Note that stratification effects are unimportant at heights

$\zeta < \zeta_s = c_N u_* / N$ (Kitaigorodskii 1992; Kitaigorodskii and Joffre 1988), and hence very near the bottom dynamical effects of stratification are negligible; here *N* is the buoyancy frequency and $c_N = 4 - 9$. In this depth range, u_* calculated from the log-layer model can be used to estimate the law-of-the-wall dissipation rate $\varepsilon_{wl}(\zeta)$, which in turn could be compared with that measured by a microstructure profiler $\varepsilon_{mc}(z)$ (z = 0 is at the sea surface; positive downward). Such comparisons permit evaluation of the efficacy of log-layer method for dissipation estimates near the seafloor.

The paper is structured as follows. Measurements and data processing are described in Section 2. Section 3 presents background tidal flow and stratification. Logarithmic approximation to the measured ADCP velocity profiles, averaged over various time scales, and the corresponding u_* estimates are discussed in Section 4. Comparison between $\varepsilon_{wl}(\zeta)$ and $\varepsilon_{mc}(z)$ in the BBL (ζ up to 5 mab) is given in Section 5, followed by a discussion in Section 6. Section 7 summarizes the results.

2. **Measurements and data processing**

The CTD, ADCP, and microstructure (MSS-60) measurements were conducted in the region of Changjiang (Yangtze) River Diluted Waters (CDW) of ECS at the mooring site P11 (30°49′N, 122°56′E; the mean depth of the water column was 38 m; see Fig. 1). Fig. 1

A bottom-mounted downward-looking RDI 1200 kHz ADCP was deployed at 0.8 mab to continuously record the along-beam velocities in mode 11 with a ping rate of 2 Hz. The mooring setup was similar to that of Cheng et al. (1999). The bin size was set to 0.02 m and the data were

ensemble-averaged over Δt = 1 s (i.e. two pings) before being recorded. Reliable ADCP data were obtained during the first 18 hours of the measurements; thereafter, because of an unexpected shift of the mounting platform, the instrument was misaligned. The velocity components u, v, and w were calculated from the original ADCP data for various averaging periods. ADCP profilers cannot deliver accurate velocity data near their transducers and near the seabed. Muste et al. (2010) found a difference between the undisturbed and the ADCP-disturbed velocities at a distance up to approximately one and a half ADCP diameter from the transducer. Mueller et al. (2007) analyzed errors of ADCP measurements depending on the deployment configuration, the ADCP diameter, and the upstream flow velocity. At 5 cm from the transducers, the bias was about 25%, but the error was less than 1% at a distance of about 50 cm. Thus, our ADCP data are reliable (the bias is less than 10%) in the range ζ = 0.04 – 0.48 mab. The shear stress was not calculated from along-beam velocities using the 'variance method' (Lu and Lueck 1999; Stacey et al. 1999), because the ADCP tilt angles (pitch and roll) exceeded the required threshold level ~ 2º (Lu and Lueck 1999).

A free-falling MSS profiler carried two airfoil shear sensors, a fast-response temperature sensor, three standard CTD sensors and an accelerometer. The sampling rate for all sensors was 1024 Hz, enabling the measurement of microscale shear with a vertical resolution of 0.006 m at a typical profiler falling speed of 0.65 m/s. The MSS measurements started on September 3 at 9 am and ended on September 4 at 10 am (local time) covering two semidiurnal tidal cycles. The hourly deployments of MSS consisted of two consecutive casts over 2 – 3 min time period. The launches were taken at a distance of about 50 – 100 m from the ADCP mooring site. The ending depth of the casts was ~ 1 – 2 mab.

The processing of MSS-60 data followed Liu et al. (2009) based on the recommendations

of the MSS developer (Prandke and Stips 1998). High-amplitude spikes in all signals were detected and removed using an iterative procedure, and the microscale shear signal was then corrected with a second order Butterworth band-pass filter. The dissipation rate ε was evaluated assuming local isotropy, i.e. $\varepsilon_{mc} = 7.5\nu\overline{(\partial u'/\partial z)^2}$. An iterative procedure was implemented for the calculation of shear variance by integrating the shear spectra at consecutive 1-m depth intervals in the wavenumber range 2 cpm < k < k_K, where $k_K = (\varepsilon/\nu^3)^{1/4}/2\pi$ is the Kolmogorov wavenumber [see Roget et al. (2006) for detailed methodology]. The MSS dissipation rate ε_{mc} varied mainly in the range $\varepsilon_{mc} = 3\times(10^{-9} - 10^{-7})$ W/kg; the minimum measured level of ε_{mc} was ~ 10^{-9} W/kg. The accuracy of the method depends on the calibration errors, frequency response limitations, variations of falling speed, non-linearity of the airfoil sensor due to changes in the angle of attack and anisotropy of the turbulence, which is discussed in detail, for example by Paka et al. (1999) and in numerous other publications (e.g., Oakey 1982; Gargett et al. 1984; Prandke and Stips 1998; Wolk et al. 2002). A combined error of the profiling measurements of ε_{mc} was about 50%.

3. Background tidal dynamics and stratification

The barotropic tidal ranges estimated from the bottom-mounted pressure gauge are shown in Fig. 2a in the background of tidal elevation $\xi_{bt}(t)$ calculated for the first week of September 2006 using the OSU Tidal Inversion Software (OTIS; Egbert and Erofeeva 2002). The measurements are in good agreement with simulations, indicating that during the period of observations the surface tidal elevation ranged between - 0.7 and 0.9 m.

Fig. 2

The OTIS barotropic tidal ellipse is shown in Fig. 2c along with the ellipses of currents

calculated using hourly averaged ADCP velocity components at several heights above the seafloor ζ = 0.04 – 0.4 mab. The measured ellipses show a semidiurnal tidal cycle (12.42 hr), superimposed by oscillations of shorter periods. The main axis of the modeled barotropic tidal ellipse is roughly oriented in the northwest-southeast direction approximately along the bottom slope (see Fig. 1); its amplitude substantially decreased (almost in half) during the second semidiurnal cycle (Fig. 2c). The bottom friction clearly affects the flow magnitude in the lower 0.4 m of the water column, but the orientation of mean flow near the seafloor remains almost the same.

The contours of specific potential density σ_θ that overlay the plot of ε values are shown in Fig. 3a; the distance from the sea surface z is given in the right axis and the height from the seafloor ζ in the left axis. Note that the averaged (over the tidal cycle) depth of the water column was 38 m. The squared buoyancy frequency across the sharp near-surface pycnocline ($z \approx 3-10$ m) was as high as $N^2 > 3\times10^{-3}$ s^{-2}, $\tau_N = 2\pi/N < 2$ min. In the main ($z \approx 10-30$ m) pycnocline of seasonal origin, the amplitude of the semidiurnal internal tide (IT) was ~ 4 m with only a minor phase shift at all depths during the first 14 hrs of the observations (Fig. 3a). Starting from $t \approx 14$ hr, the main pycnocline splits at $z \approx 22$ m, forming a depression in deeper water and an elevation at shallower levels. This could have resulted from an energetic second mode of internal tide or advection of different water masses by tidal currents. Indeed, an intrusion of warmer saltier water is well identifiable in isopycnal coordinates in Fig. 3b between t = 15 and 23 hrs above σ_θ = 23.0, which is marked by a dashed horizontal line. Below σ_θ = 23.0, T and S at the isopycnal surfaces do not change during entire 25 hrs of profiling, suggesting internal waves as the major mechanism that influences stratification in the lower part of the water column.

Fig. 3

The main features of the turbulent kinetic energy dissipation rate shown in Fig. 3a are consistent with the details of stratification. Lee et al. (2006) and Matsuno et al. (2006) reported first dissipation measurements along hydrographic transects in the outer shelf area of ECS about 150 miles to the north-east and south-east from the CDW region and Liu et al. (2009) first analyzed temporal variations of the dissipation rate in the Yellow Sea at 35ºN. The vertical structure of turbulence observed at the test site is typical for shallow waters in tidal and non-tidal coastal zones (e.g., Simpson et al. 1996; Lozovatsky and Fernando 2002; Rippeth and Inall 2002; MacKinnon and Gregg 2003; Palmer et al. 2008). The near-surface turbulence with highest ε ($> 10^{-6} - 10^{-7}$ W/kg) sometimes penetrated to the pycnocline, much like "turbulent chimneys" at t = 6 – 7 and 16 – 17 hrs. A clear minimum of ε existed at the mid depths, and this region was not affected by the turbulence of surface and bottom boundary layers. The dissipation rate generally increases from the mid-depth toward the seafloor, where rotating tidal flow generates turbulence in the BBL at typical heights up to 2 – 5 mab. The height of the turbulent boundary layer was mainly governed by the magnitude of the tidal flow (Lozovatsky et al. 2008a), but it can also be affected by other processes. A local maximum of the dissipation rate can be seen at ζ = 9 – 16 mab, which is evident in individual dissipation profiles given in Section 5 (Fig. 8). It is possible that this maximum is associated with enhanced local shear at the upper boundary of the weakly stratified BBL. The BBL height h_B varied in time between z = 27 and 22 m (ζ = 11 – 16 mab); (see Fig. 3a and a combined plot of individual $T(z)$ and $S(z)$ profiles in Fig. 4). The enhanced shear at h_B could also be related to a so-called near-bottom current 'jet' associated with a velocity maximum that develops a few meters above the seafloor. Various processes potentially responsible for a near-bottom 'jet' in ECS, including the interactions of tidal flow with internal waves of various frequencies or inertial oscillations related to the rotating tidal vector, are

Fig. 4

discussed in Lozovatsky et al. (2008a).

4. The log-layer approximation to the velocity profile U (ζ = 0.04 – 0.48 mab)

The horizontal velocity $U(\zeta)$ is assumed to satisfy the logarithmic model

$$U(\zeta) = (u_*/\kappa)\log(\zeta/\zeta_0) \tag{1}$$

near the bottom, provided that the flow is steady, fully developed, non-stratified and parallel. If Eq. (1) fits experimental data, then the friction velocity u_* and aerodynamic roughness ζ_0 can be estimated and the dissipation rate based on the law-of-the-wall

$$\varepsilon_{wl}(\zeta) = cu_*^3/\kappa\zeta \ , \tag{2}$$

can be calculated assuming a local balance between the shear production and viscous dissipation of turbulent kinetic energy; $c \sim O(1)$.

A tidal current, being a non-steady flow, cannot formally satisfy many of these requirements. In spite of such restrictions, logarithmic-like velocity profiles are often observed in a variety of natural currents (e.g., Schauer 1987; Elliott 2002; Moum et al. 2002, 2004; Liu, Wu et al. 2009), although, as pointed out earlier, u_* obtained via fitting velocity profiles to (1) and that based on eddy correlations (Friedrichs and Wright 1997; Howarth and Souza 2005; Lozovatsky et al. 2008b) do not agree for thick BBL (h_B ~ 10 m). This is probably due to the violation of assumptions underlying the law-of-the-wall parameterization (Li 1994; Smith and McLean 1977). In addition, the presence of stable stratification (e.g., Lien and Sanford 2004; Perlin et al. 2005) and the details of bottom roughness and corresponding form drag (Li 1994; Sanford and Lien 1999; Edwards et al. 2004) also contribute to the disparity. Lozovatsky et al. (2008b) present further discussions on this issue with application to ECS shelf.

In geophysical flows, the log-layer lies below a height where the effect of rotation begins to be important (Lueck and Lu 1997). The lower boundary of the log-layer is proportional to ν/u_* but the upper boundary is formally undefined, because the law-of-the-wall (2) is specified by a single governing parameter u_*, which prevents formulation of a characteristic length scale. In a reversing channeled tidal flow with semidiurnal tidal frequency ω_T, Lueck and Lu (1997) found a departure of the velocity profile from the log-layer approximation (for boundary layers thicker than 3.6 m) at the height $h_\omega = c_\omega(u_*/\omega_T)$, where c_ω = 0.04. The height of log-layer is expected to be less than the depth of the well-mixed bottom boundary layer, which in turn can be scaled as $h_f = c_f(u_*/f)$ or $h_N = c_N(u_*/N)$, or $h_{Nf} = c_{Nf}\left(u_*/\sqrt{Nf}\right)$, where f and N are the inertial and buoyancy frequencies, respectively; see Lozovatsky et al. (2005). The most popular values for the nondimensional constants are c_f = 0.4 (e.g., Weatherly and Martin 1978, and many others), c_{Nf} = 0.5 – 1.3 (Zilitinkevich and Esau 2002; Weatherly and Martin 1978) and c_N = 4 – 9 (Kitaigorodskii 1992). The following estimates can thus be made on the upper limit of the log-layer height at the test site: h_f = 22 m, h_N = 4 – 7 m, h_{Nf} = 20 – 51 m, and h_ω = 1.1 m for characteristic values u_* ~ 0.004 m/s, $N = 5\times10^{-3}$ s^{-1}, $f = 7.2\times10^{-5}$ s^{-1}, and $\omega_T = 1.4\times10^{-4}$ s^{-1}. Note that the estimate of h_ω may not be suitable for our measurements taken on the open shelf in a rotating, but not oscillating channeled tidal flow, for which the formula $h_\omega = 0.04(u_*/\omega_T)$ was derived. A typical log-layer height reported for shallow tidal flows varies between 3 – 5 and 10 – 15 m, extending sometimes up to ~ 20 mab (Lueck and Lu 1997; Sanford and Lien 1999; Elliott 2002; Lozovatsky et al. 2008a).

The original velocity data contained higher-frequency fluctuations caused by various small-scale processes and noise. To obtain mean velocities uninfluenced by natural temporal

variations of smaller scales, the original records were run-averaged over consecutive overlapped segments of the specified length $\tau/\Delta t$, where $\Delta t = 1$ min. Several examples of velocity profiles $U_{(\tau=10)}(\zeta)$ averaged over τ = 10 min are given in Fig. 5. The measurements are well approximated by the least-squared logarithmic fits especially for the periods of relatively large velocity magnitudes. Note that the values of ζ_0 were very small (mainly in the range $10^{-4} - 10^{-5}$ m) and so is the physical bottom roughness. The estimates of ζ_0 are very sensitive to the accuracy of the fit. At several segments of the imperfect log fit ζ_0 became almost zero, which is not unusual in oceanographic research (e.g., Bowden, 1978), but this may lead to higher uncertainty of u_* estimates.

Fig. 5

To investigate the effects of the averaging time scale τ (Soulsby, 1980) on the measurement of mean velocity near to the seafloor, $U_\tau(\zeta) = \left[u_\tau^2(\zeta) + v_\tau^2(\zeta)\right]^{1/2}$ was evaluated using a set of τ = 5, 10, 15 min, which covers the time range between a pair of hourly MSS casts. These short averaging periods are expected to present a quasi-stationary state of the barotropic tide near the seafloor.

The goodness of the log-fits for individual $U_\tau(\zeta)$ profiles was evaluated by the coefficient of determination r^2. The cumulative distribution functions CDF(r^2) (Fig. 6) indicate that a logarithmic model with all selected τ is suitable ($r^2 > 0.8$) for almost all cases. Short averaging scales τ = 5 – 15 min led to a larger percentage of good ($r^2 > 0.8$), but not excellent ($r^2 > 0.95$) fits, with 20% < CDF < 40% for $0.8 < r^2 < 0.95$.

Fig. 6

To estimate the time scales that start affecting the applicability of log-fits to the skin layer flow of rotating tide of relatively small variability in magnitude, much longer τ = 30, 60, 90, and 120 min were used to calculate the corresponding r^2. The τ = 30 min averaging improves the

goodness of the fits with CDF < 10% for $r^2 < 0.95$ and an approximate saturation of CDFs began at τ = 60 min with a very little change for τ = 90 and 120 min. It is obvious that an increase of the averaging time leads to a reduction of small-scale fluctuations in the mean velocity profile, but on the other hand a tidal flow at 60 - 120 min segments, can hardly be considered as quasi-steady. It is, however, plausible that the assumptions of parallel flow and stationarity are less restrictive in determining force balance in the near-bottom skin layer of slowly rotating tidal flow. The time scales of changes of mean velocity is also slow, several tens of minutes if not hours for the vector magnitude (see the only slightly stretched empirical ellipses in Fig. 2b) compared to turbulence time scales of several minutes. Thus the assumption $\partial U/\partial t << \partial\overline{u'w'}/\partial z$ facilitates the conditions necessary for the law-of-the-wall. Alternatively, one may argue that the observed logarithmic profiles are corresponding to some yet-to-be identified dynamics and not related to the canonical law-of-the-wall; however, if this hypothesis is correct, we expect the coefficient κ to be very different from the classical value of the von Karman constant.

5. Turbulence near the seafloor (MSS and ADCP-based dissipation profiles)

The friction velocities u_* obtained from Eq. (1) vary in the range ~ (1 – 7)×10^{-3} m/s for cases where the principal semidiurnal tidal constituent is superimposed by irregular shorter-period oscillations (period ~ 40 – 50 min and amplitude ~ 0.5×10^{-3} m/s; Fig. 7a). The Fig. 7 drag coefficient $C_D = u_*^2/U_{(1)}^2$ is shown in Fig. 7b, where the mean velocity $U_{(1)}$ at ζ = 1 mab (Ludwick 1975; Bowden 1978; Elliott 2002) was calculated based on that measured at ζ = 0.48 mab using the log-layer model (1). The mean value of $\overline{C}_D = 2.2\times10^{-3}$ is in general agreement with common estimate $C_D = 2.5\times10^{-3}$ (e.g., Thorpe 2005). The mean ratio $\overline{u_*/U_{(0.48)}} = 0.046$

is close to the estimate of $\overline{u_*/U_{(0.45)}} = 0.041$ obtained on a shallow shelf near the Jiaozhou Bay of ECS (Lozovatsky et al. 2008b) for $U(\zeta = 0.45$ mab) as well as the ADV-based eddy correlation estimates of u_*. It is not unusual that C_D varies substantially in tidal flows, especially in rotating tidal currents (e.g., Green and McCave 1995; Elliot 2002; Lozovatsky et al. 2008b). Mobile bed forms, time-varying flow, and the lack of equilibrium between flow and seabed (Ludwick 1975; Cheng et al. 1999) are some possible causes of non-constant C_D.

The estimates of u_* based on 10- and 30-min averaged velocity profiles were used to calculate the law-of-the-wall dissipation profiles $\varepsilon_{wl}(\zeta)$ (Eq. 2) at the times of MSS casts. The corresponding segments of $U_{(\tau=10)}$ and $U_{(\tau=30)}$ were centered at the beginning of each hour to be consistent with the MSS measurements taken each hour 2 – 3 min apart. The dissipation estimates from two consecutive MSS casts were averaged at each depth and the resulting $\varepsilon_{mc}(\zeta)$ profiles were compared with $\varepsilon_{wl}(\zeta)$. Because the measurements were taken in a rotating tidal flow, $c = 1.5$ was used in Eq. (2), following Lozovatsky et al. (2008b).

Eight of the 18 pairs of $\varepsilon_{mc}(\zeta)$ and $\varepsilon_{wl}(\zeta)$ profiles are shown as examples in Figs. 8 (a – d) for the time periods where the flow was directed south, north, east, and west during one and a half semidiurnal tidal cycles. For cases other than $t = 6$, 7, and 17 hrs (westward upslope flow), $\varepsilon_{mc}(\zeta)$ and $\varepsilon_{wl}(\zeta)$ are consistent at a specific height ζ close to the lower end of the MSS profiles. In some cases ($t = 4$, 9, 12, 15 hrs) the two profiles are matching so that $\varepsilon_{wl}(\zeta)$ can be construed as a continuation of $\varepsilon_{mc}(\zeta)$ down to the very bottom. For $t = 10$ and 13 hrs (Figs. 10b, c) the profiles do not intersect, but the trends of MSS profiles indicate the possibility of coincidence of $\varepsilon_{mc}(\zeta)$ and $\varepsilon_{wl}(\zeta)$. In general, the agreement between $\varepsilon_{mc}(\zeta)$ and $\varepsilon_{wl}(\zeta)$ is

Fig. 8

good, considering the myriad of uncertainties related to instrument accuracy, assumptions involved, data processing methodology, and natural short-period intermittency of the dissipation rate. This agreement corroborates the fairness of the assumptions of constant momentum flux and the local equilibrium between shear production and viscous dissipation of turbulent kinetic energy near the seafloor in rotating tidal flow over time scales 10 – 30 min. The height of variability of the law-of-the-wall, which we defined as a point of the actual or expected intersection of the MSS and ADCP dissipation profiles, varies from 2 – 3 mab (t = 9 and 10 hrs) to 4 – 6 mab (t = 4 and 15 hrs) for $u_* = (4-6)\times 10^{-3}$ m/s.

The shear induced turbulence near the seafloor dominates most of the rotating semidiurnal cycle, but when the flow turns west (Fig. 8d) the shear production becomes weak due to substantial reduction of tidal velocity (see Fig. 5, t = 17, 6, and 7 hrs, where the mean U is less than 0.06 m/s). When the ambient flow magnitude drops below this level, the log-layer approximation ceases to be valid, so does the accuracy of friction velocity and dissipation estimates. The worst agreement between $\varepsilon_{mc}(\zeta)$ and $\varepsilon_{wl}(\zeta)$ is seen in Fig. 8d, where almost constant ε (~ (3 – 4)×10^{-8} W/kg at t = 6 hr and ~ (6 – 8)×10^{-8} W/kg at t = 17 hr) extends up to 9 – 10 mab indicating an external source of turbulent kinetic energy in the middle of the water column.

6. Discussion: A distant source of turbulence?

6a. *Effect of internal waves*

The MSS measurements of ε and that calculated based on u_* using the law-of-the-wall showed the applicability of the latter to CDW region of ECS shelf for all phases of the tidal flow except for the periods when the flow was generally westward. During this phase (t = 6, 7, and 17

hrs), the smallest values of $u_* \approx 10^{-3}$ m/s (Fig. 7a) were noted and hence weak boundary layer turbulence [$\varepsilon_{wl}(\zeta = 0.04 \text{ mab}) = (3 - 8)\times 10^{-8}$ W/kg] was produced near the seafloor. The $\varepsilon_{mc}(\xi)$ between the dissipation maximum near h_B and the seafloor in this case was more than an order of magnitude larger than $\varepsilon_{wl}(\xi)$ (Fig. 8d). This could be related to the small bathymetric irregularities of the area (about tens or hundreds meters wide and a few meters height) that are not resolved by available bathymetric data (Fig. 1). The angle of the characteristics of IT $\beta = \sqrt{\omega_T^2 - f^2 / N^2 - f^2} \approx 2.4 \times 10^{-2}$ is larger than the averaged bottom slope toward the coast, $\alpha_{sl} \approx 1.4 \times 10^{-3}$, thus preventing direct generation of bottom turbulence by IT at the site (Kunze and Llewellyn Smith 2004). However, a localized remote topographic rise over the main plain of the seafloor (mean depth ~ 50 m), located at 30.75°N, 132.14°E with a summit z = 25 m below the sea surface (Fig. 1), could have played a role in the generation of high dissipation at depths z = 25 – 35 m. The approximate radius of this rise is about 2.5 – 3 km between 25 and 35 m isobaths. At this depth, the rise is located at a distance dx ~ 15 km to the test site (see details in Fig. 1). The notion of the generation of a permanent turbulent zone surrounding the rise that extends or shrinks depending on the phase of the tidal cycle is explored next. This turbulence can be transported to the test site by the westward barotropic tidal and non-tidal currents. Propagating tidal and shorter-period internal waves may also produce turbulence (e.g., Lozovatsky et al. 2003, Lee et al. 2006), and thus enhanced dissipation at the test site. Nonlocal effects so induced cause violation of assumptions underlying the law-of-the-wall.

To substantiate this hypothesis, the depth (H) integrated internal tide generating body force $F = \frac{\bar{Q}}{\omega_T} \nabla \frac{1}{H} \int_0^H N^2 z dz$ (Baines 1982) was calculated to locate the likely hotspots of internal tide generation in the region (e.g., Merrifield and Holloway 2002; Sherwin et al. 2002; Niwa and

Hibiya 2004; Green et al. 2008); here $\vec{Q} = (Hu_T, Hv_T)$ is the barotropic tidal transport. Analyzing SAR images, Azevedo et al. (2006) and da Silva et al. (2009) showed that not only IT but also packets of non-liner internal waves (NLIW) are often generated at those bathymetric hotspots where F is large ($F > 0.25$ m^2/s^2). The IT generating body force F was calculated using the OTIS tidal current vectors (http://volkov.oce.orst.edu/tides), the measured buoyancy frequency profile at the test site and the water depth based on a high-resolution local bathymetry database. The spatial variation of stratification was assumed to be insignificant within a relatively small region surrounding the test site, and hence the tidally averaged buoyancy frequency was taken as representative to the entire region. Historical hydrographical data in the region support this assumption (not shown).

The results shown in Fig. 9 indicate that internal waves can be induced over the flanks of the bathymetric rise and propagate away, which can be a likely source of topography-related turbulence. Internal tidal waves that are generated at the ocean shelf break of ECS propagate northwest toward shallower waters. Manifestation of intense NLIW packets with a phase speed of about 1.6 m/s has been observed before the emergence of low tide in ECS, northeast of the CDW region (Lee et al. 2006). Figure 9 affirms that IT and NLIW can be generated much closer to the coast at localized topographic features such as a bathymetric rise near our test site, and therefore the phenomenon reported by Lee et al. (2006) may very well exist there. As such, topographic turbulence around the rise can be transported by NLIW (together with the westward directed tidal current) to the test site (P11). In addition, the radiated internal waves can degenerate at some distance from the rise, forming enhanced turbulence such as that seen near P11. The latter has been observed in the Yellow Sea (Liu et al. 2009), where the dissipation rate of NLIW-induced turbulence is increased by an order of magnitude. This scenario may explain

Fig. 9

the observations of enhanced dissipation (Fig. 8d) in the proximity of the low phase of barotropic tide in ECS (Lee et al. 2006).

6b. ***Topographic turbulence***

Because there are no microstructure measurements in the turbulent zone surrounding the bathymetric rise, or as we call it a small 'seamount', the dissipation rate $\varepsilon(x)$ with distance x from the source cannot be directly evaluated. Nevertheless, some estimates are possible using indirect comparisons with similar turbulent zones elsewhere, wherein the dissipation measurements have been taken at different distances from seamounts and small islands listed in Section A1 of the Appendix.

For example, a turbulent zone was observed in the upper ~ 100 m layer, west of the Baker Island (Fig. 10a), in Equatorial Surface Current, while near the Castor seamount (Fig. 10b) it was generated by a superposition of tidal flow and a weak southwestern non-tidal current (Korotenko 1995). East of the Howland Island (not shown here) turbulence was produced by the Equatorial Undercurrent and the Irving seamount turbulent zone above and away from its summit was due to the interaction of internal tide with bathymetry (Lavelle et al. 2004). Fig. 10

The estimates of $\bar{\varepsilon}$ averaged over the thickness of each turbulent zone (see Appendix, Section A1 for details) are shown in Fig. 11 as a function of the distance x from the summits or edges of the obstacles. In all five turbulent zones, $\bar{\varepsilon}(x)$ roughly follows $\bar{\varepsilon} \sim Cx^{-1}$, where the dimension of C is [m^3 s^{-3}], which can be considered as cube of a characteristic velocity u_o. Therefore, Fig. 11

$$\bar{\varepsilon}(x) = u_o^3 x^{-1}. \tag{3}$$

The characteristic velocity u_o depends on a number of factors, including velocity of the

impinging flow, the dynamics of generated internal waves, small-scale topographic roughness (Kunze and Toole 1997) and other factors. Figure 11 shows a high dissipation rate (approaching $\sim 7\times10^{-9}$ W/kg), sometimes to a distance of ~ 20 km from all bathymetric features *regardless* of the mechanism of turbulence generation (e.g., quasi unidirectional or rotating tidal flows).

A conservative estimate can be made using (3) with the lowest $u_o = 3.5\times10^{-2}$ m/s for the "source dissipation" $\bar{\varepsilon}_o$ (around the bathymetric rise) at approximately 15 km southeast from the test site. For $\bar{\varepsilon} \approx (3-7)\times10^{-8}$ W/kg in the BBL at the slope (see Fig. 8d), $\bar{\varepsilon}_o \approx (5-10)\times10^{-7}$ W/kg at x = 1 km from the approximate center of the rise. It is ten times higher near (x = 0.1 km) the center. These are reasonable numbers for topographically induced turbulence near the source, and consistent with Lueck and Mudge (1997), who showed $\bar{\varepsilon}_o > 10^{-6}$ W/kg near the summit of seamount Cobb and the dissipation rates above 10^{-7} W/kg at a distance of 12 – 14 km from the summit. Therefore, reckoned topographically induced turbulence around the bathymetric rise in the CDW region is high enough to explain the observed enhancement of the dissipation rate at the test site in the presence of IT, non-linear internal waves, and a westward directed barotropic tidal current.

The empirical power law (3) shown in Fig. 11 can be supported by the following theoretical consideration. Any property of a turbulent zone of thickness h_{tz} at a distance x behind an obstacle (seamount or island) of diameter D, say it being the dissipation rate $\bar{\varepsilon}$ (averaged over h_{tz}), can be written as

$$\bar{\varepsilon} = \bar{\varepsilon}(U_0, h_{tz}, D, x, N_0, z_r, \nu), \tag{4}$$

where x is the downstream distance, U_0 and N_0 are characteristic flow velocity and buoyancy frequency, respectively, z_r is the roughness parameter and ν the kinematic viscosity (e.g.,

Brighton 1978). Note that h_{tz} itself is affected by the ratio between the obstacle height and the water depth. This general dimensional analysis allows relevant processes such as turbulence and internal wave generation. Therefore, it is possible to write

$$\bar{\varepsilon} = \frac{U_0^3}{x} f\left(\frac{U_0}{N h_{tz}}, \frac{U_0 D}{\nu}, \frac{h_{tz}}{D}, \frac{h_{tz}}{z_r}, \frac{x}{D} \right) \tag{5}$$

where f is a function. The values of the first three variables are listed in Table 1 for the Baker Island and for the case in point. In the table, the present bathymetric feature is assumed to be subjected to $U_0 \approx 0.2 - 0.3$ m/s (velocity of the westward barotropic current at t = 6, 7, and 17 hrs; see U_{bt} in Fig. 2a), $N_0 = 2.2 \times 10^{-2}$ s^{-1}, h_{tz} = 10 m between z = 25 and 35 m, and $D \approx 6$ km (at z = 30 m). For the Baker Island $U_0 \approx 0.2$ m/s (Lilover et al. 1993), $N_0 \approx 8 \times 10^{-3}$ s^{-1} (Lozovatsky 1996), h_{tz} = 30 m, D = 2.6 km in the depth range 50 – 80 m.

Table. 1

Note that the values of the turbulent zone Froude number $Fr_{tz} = U_0 / N h_{tz}$ are close to unity in both cases, suggesting strong internal wave activity. Because of large Reynolds numbers $Re_{tz} = U_0 D / \nu$ involved, dependence on it can be neglected (Reynolds number similarity). The ratio h_{tz}/D is very small suggesting little sensitivity of turbulence to this parameter at large x (e.g., Xu et al. 1995). Thus Eq. (5) for the present and Baker Island cases becomes

$$\bar{\varepsilon} = \frac{U_0^3}{x} f_1(x/D), \tag{6}$$

where f_1 in general depends on h_{tz}/D, Fr_{tz}, and h_{tz}/z_r, but this dependence is inconsequential for the cases considered here.

Measurements have shown that $\bar{\varepsilon} \sim x^{-1}$ (see Fig 11), indicating that f_1 is independent of x/D. Therefore

$$\bar{\varepsilon} = C\frac{U_0^3}{x}, \tag{7}$$

where $C = C\left(Fr_{tz},\, h_{tz}/D,\, h_{tz}/z_r\right)$ is a constant that can be evaluated using the Baker Island data. The normalized mean dissipation $\bar{\varepsilon}/\left(U_0^3/x\right)$, shown in Fig. 12 as a function of the normalized distance x/D west of the island, suggests C = 0.03, which can be used to estimate $\bar{\varepsilon}$ at the test site in ECS, west of the CDW 'seamount'. The barotropic velocity of tidal flow $U_0 \approx 0.2 - 0.3$ m/s and constant C accounts for all other processes of turbulence generation, including internal tide and non-linear internal waves, its horizontal diffusion, and transport. Formula (7) gives $\bar{\varepsilon} \approx \left(1.6 - 5.4\right)\times 10^{-8}$ W/kg. These values of $\bar{\varepsilon}$ are in agreement with the MSS dissipation rates shown in Fig. 8d for ζ < 9 – 11 mab (the depth range between z = 27 – 29 m and the seafloor). It was argued that turbulence therein is caused by nonlinear waves and to a lesser degree by wall/bottom shear. The analysis given above provides further support for this hypothesis, which is also supported by the observed alteration of temperature and salinity in the BBL (Appendix, Section A2) during the western and southwestern phases of tidal flow, which is a recurring process.

Fig. 12

7. Summary

The TKE dissipation rate profiles measured near the seafloor of the East China Sea (CDW region) by an MSS microstructure profiler over two semidiurnal cycles $\varepsilon_{mc}\left(\zeta\right)$ were compared with those evaluated using the law-of-the-wall $\varepsilon_{wl}\left(\zeta\right)$ (Eq. 2). In the latter, the friction velocity u_* was deduced by fitting the classical logarithmic velocity profile to the ADCP data very near the bottom (ζ = 0.04 – 0.4 mab), thus ensuring the absence of stratification effects. The

sensitivity of u_* to various averaging time scales was tested, and averaging over 30 min segments provided the highest coefficient of determination for log-layer fits, being at the same time consistent with the assumption of quasi-stationary state of tidal flow over sufficiently short time periods. The u_* during the tidal cycle was found to be in the range $(1 - 7)\times10^{-3}$ m/s and the mean value of the ratio $\left\langle u_*/U_{(\tau=30)}\right\rangle$ = 0.041. The law-of-the-wall dissipation profiles generally intersected with MSS profiles at ζ = 2 – 5 mab, suggesting the applicability of the law-of-the-wall for shallow tidally-affected waters with an averaging time of about 30 min. When turbulence in the bottom boundary layer is influenced by external (non-local) sources, the level of dissipation can be substantially higher than $\varepsilon_{wl}(\zeta)$. Assuming that non-local bathymetry plays a role in enhancing $\varepsilon_{mc}(\zeta)$ [compared to $\varepsilon_{wl}(\zeta)$] in the lower 7 – 10 m of the water column during the upslope (westward) phase of tidal currents in CDW region, it was hypothesized that the interaction of tidal flow with a bathymetric rise to the east of the observational site was responsible for producing and radiating energetic internal waves that degenerate into turbulence. This leads to enhanced dissipation within BBL on the slope, compared to that reckoned from the law-of-the-wall.

The comparison of the present case with the dissipation measurements in turbulent zones around other seamounts and small islands shows that enhanced dissipation in the BBL at the test site could be interpreted quantitatively on the premise that the internal tide and nonlinear internal waves, aided by the westward barotropic tidal component, generate and transport turbulence upslope for distances as much as 15 km (to the test site). This is further supported by the observations of Lee et al. (2006) that show how solitary internal waves in ECS generate turbulence during the course of propagation, which can enhance dissipation levels over substantial distances from the source. Examples given in Section 6b indicate that

internal-wave-generated turbulence at isolated topographic features in deep or shallow oceans can occupy extensive areas, where topography-related turbulence horizontally diffuses and can be transported long distances. The flow around a small 'seamount' in the CDW region of ECS may have a hydrodynamic similarity with those (Fig. 11), based on which $\bar{\varepsilon}(x)$ were estimated surrounding the seamount (rise) and infer its influence on the dissipation within the BBL upslope to the west. Note that when the tidal currents change direction, the internal wave propagation toward the test site is impeded so is the enhancement of turbulence at the test site. Under such conditions, the log-law based dissipations estimates are expected to be valid.

Appendix

A1.

In section 6b, we explore the data obtained by Russian oceanographers with the participation of the first author using a "Baklan" microstructure profiler (Paka et al. 1999) and a lowered ADCP (Lilover et al. 1993; Lozovatsky 1996) at the seamounts Ampere (φ = 12°53'W, λ = 35°03'N; the summit is at a depth z_{sm} ~ 60 m), Irving (30.87°N, 28.65°W; z_{sm} ~ 265 m) and Castor (a small pinnacle atop of the Great Meteor central summit plain at its southern tip, 29.44°N, 29.26°W; z_{sm} ~ 270 m) in the Eastern Atlantic and two small equatorial islands in the equatorial Pacific - the Baker (0°11.5'N, 176°29'W) and the Howland (0°48.1′N, 176°38.05′W) islands. The summits of Ampere and Castor are also small, ~ 2 – 3 km in diameter (Nabatov and Ozmidov 1988; Gibson et al. 1993; Korotenko 1995; Mohn and Beckmann 2002), but Irving summit is larger, approximately 5 over 9 km (Lozovatsky 1999; Lavelle et al. 2004). The diameter of the Baker Island at the sea surface is ~ 1 km; the short E-W axis of the Howland Island is about the same size, but its long NNW-SSE axis is ~ 2 km (Lilover et al. 1993).

Despite the differences of mesoscale dynamics around the selected bathymetric features

(persistent currents in the Equatorial Pacific vs. dominant tidal flows in the Eastern Atlantic) extended turbulent zone were always generated around these topographies.

To investigate how the averaged dissipation rate over the depth of a turbulent zone $\bar{\varepsilon}$ vary with the distance from these topographic features, we selected the depth range Δz = 50 – 80 m for the Baker Island [the upper ~ 50 m of the water column were affected by surface processes, Fig. 10a], Δz = 120 – 170 m for the Howland Island [from the upper boundary of the turbulent zone to the maximum profiling depth], Δz = 30 – 65 m for Ampere seamount [between the summit floor and the bottom of the wind-affected upper layer (Gibson et al. 1993)], Δz = 145 – 195 m for the Castor seamount (the choice is evident from Fig. 10b), and Δz = 90 – 140 m for seamount Irving [mid portion of the turbulent column generated above the summit].

A2.

The alteration of temperature and salinity in the BBL, which was observed during the western and southwestern phases of tidal flow, is also consistent with the hypothesis of the advective origin of the enhanced turbulence in the BBL observed at the test site during the phase of the western directed tidal flow. Between t = 13 and 17 hrs, T and S in the BBL (below h_B, which is depicted in Fig. 4) continuously increased/decreased with time (from 21.17 to 21.34^{o}C and from 33.75 to 33.63 psu) indicating advection of warmer fresher water to the test site. This water could not be transported onshore along the seafloor from deeper depths, where temperature is lower and salinity is higher, although it could be advected from shallower depths. The bathymetric rise shown in Fig. 1 to the east of the test side is the only region where warmer and less saline water can be found near the bottom. For $\varepsilon_{mc}(\zeta)$ pertinent to other sectors of tidal flow, this topographic effect does not influence the law-of-the-wall dissipation rate, which is

consistent with the undisturbed dissipation values at upper levels. Note that it is a recurring process, with approximately the tidal period, and thus the observed effect should not emerge during one tidal excursion but exist in a quasi stationary state for the time of relatively persistent stratification in the region.

Acknowledgements

The authors are grateful to scientists and students at Ocean University of China led by Prof. Hao Wei for arranging logistics of data collection. The effort was supported by the Major State Program of China for Basic Research (grant No. 2006CB400602). The analysis presented in this paper was supported by the US Office of Naval Research (grant N00014-05-1-0245), the National Natural Science Foundation of China (Z. Liu, grants 41006017 and 41076001), the Fundamental Research Funds for the Central Universities (Z. Liu, grant No. 2010121031), Arizona State University (J. Armengol as a visiting researcher), and by the Spanish Ministry of Education and Science (E. Roget, grant FIS2008-03608).

References

Azevedo A, da Silva JCB, New AL (2006) On the generation and propagation of internal solitary waves in the southern Bay of Biscay. Deep-Sea Res I 53:927–941.

Baines PG (1982) On internal tide generation models. Deep-Sea Res A 29:307–338.

Bowden KF (1978) Physical problems of the benthic boundary layer. Geophys Surveys 3:255–296.

Brighton PWM (1978) Strong stratified flow past three-dimensional obstacles. Q J Roy Meteorol

Soc 104:289–307.

Cheng RT, Ling CH, Gartner JW (1999) Estimates of bottom roughness length and bottom shear stress in South San Francisco Bay, California. J Geophys Res 104:7715–7728.

da Silva JCB, New AL, Magalhaes JM (2009) Internal solitary waves in the Mozambique Channel: Observations and interpretation. J Geophys Res 114:C05001. doi:10.1029/2008JC005125.

Edwards KA, MacCready P, Moum JN, Pawlak G, Klymak JM, Perlin A (2004) Form drag and mixing due to tidal flow past a sharp point. J Phys Oceanogr 34:1297–1312.

Egbert GD, Erofeeva SY (2002) Efficient inverse modeling of barotropic ocean tides. J Atmos Oceanic Tech 19:183–204.

Elliott AJ (2002) The boundary layer character of tidal currents in the Eastern Irish Sea. Estuar Coast Shelf Sci 55:465–480.

Foster DL, Beach RA, Holman RA (2000) Field observations of the wave bottom boundary layer. J Geophys Res 105:19634–19647.

Friedrichs CT, Wright LD (1997) Sensitivity of bottom stress and bottom roughness estimates to density stratification, Eckernförde Bay, Southern Baltic Sea. J Geophys Res 102:5721–5732.

Gargett AE, Osborn TR, Nasmyth PW (1984): Local isotropy and the decay of turbulence in a stratified fluid. J Fluid Mech 144:231–280.

Gibson CH, Nabatov V, Ozmidov R (1993) Measurements of turbulence and fossil turbulence near Ampere seamount. Dynam Atmos Ocean 19:175–204.

Green JAM., Simpson JH, Legg S, Palmer MR (2008) Internal waves, baroclinic energy fluxes

and mixing at the European shelf edge. Cont Shelf Res 28:937–950.

Green MO, McCave IN (1995) Seabed drag coefficient under tidal currents in the eastern Irish Sea. J Geophys Res 100:16,057–16,069. doi:10.1029/95JC01381.

Howarth MJ, Souza AJ (2005) Reynolds stress observations in continental shelf seas. Deep-Sea Res II 52:1075–1086.

Kitaigorodskii SA (1992) The location of thermal shelf fronts and the variability of the heights of thermal boundary layers. Tellus A 44:425– 433.

Kitaigorodskii SA, Joffre SM (1988) In search of a simple scaling for the height of the stratified atmospheric boundary layer. Tellus A 40:419– 433.

Korotenko KA (1995) On the formation of mesoscale inhomogeneities of the matter concentration field in a local upwelling zone of the ocean. Oceanology English Translation 34(4):445–451.

Kunze E, Toole JM (1997) Tidally driven vorticity, diurnal shear, and turbulence atop Fieberling Seamount. J Phys Oceanogr 27:2663–2693.

Kunze E, Llewellyn Smith SG (2004) The role of small scale topography in turbulent mixing of the global ocean. Oceanography 17:51–60.

Lavelle JW, Lozovatsky ID, Smith IV DC (2004) Tidally induced turbulent mixing at Irving Seamount—modeling and measurements. Geophys Res Lett 31:L10308. doi:10.1029/2004GL019706.

Lee JH, Lozovatsky I, Jang ST, Jang CJ, Hong CS, Fernando HJS (2006) Episodes of nonlinear internal waves in the northern East China Sea. Geophys Res Lett 33:L18601.

doi:10.1029/2006GL027136.

Li MZ (1994) Direct skin friction measurements and stress partitioning over movable sand ripples. J Geophys Res 99:791–799.

Lien RC, Sanford TB (2004) Turbulence spectra and local similarity scaling in a strongly stratified oceanic bottom boundary layer. Cont Shelf Res 24:375–392.

Lilover M, Lozovatsky ID, Gibson CH, Nabatov VN (1993) Turbulent exchange through the Equatorial Undercurrent core of the Central Pacific. J Mar Syst 4:183–195.

Liu H, Wu C, Xu W, Wu J (2009) Contrasts between estuarine and river systems in near-bed turbulent flows in the Zhujiang (Pearl River) Estuary, China. Estuar Coast Shelf Sci 83:591–601.

Liu Z, Wei H, Lozovatsky ID, Fernando HJS (2009) Late summer stratification, internal waves, and turbulence in the Yellow Sea. J Mar Syst 77:459–472.

Lozovatsky ID (1996) Turbulence decay in stratified and homogeneous marine layers. Dynam Atmos Ocean 24:15–25.

Lozovatsky ID (1999) Seamount turbulence: Generation and decay. Abstracts of XXII General Assembly of IUGG, Birmingham, UK.

Lozovatsky ID, Fernando HJS (2002) Turbulent mixing on a shallow shelf of the Black Sea. J Phys Oceanogr 32:945–956.

Lozovatsky ID, Morozov EG, Fernando HJS (2003) Spatial decay of energy density of tidal internal waves. J Geophys Res 108:3201. doi:10.1029/2001JC001169.

Lozovatsky I, Figueroa M, Roget E, Fernando HJS, Shapovalov S (2005) Observations and

scaling of the upper mixed layer in the North Atlantic. J Geophys Res 110:C05013. doi:10.1029/2004JC002708.

Lozovatsky ID, Liu Z, Wei H, Fernando, HJS (2008a) Tides and mixing in the northwestern East China Sea Part I: Rotating and reversing flows. Cont Shelf Res 28:318–337.

Lozovatsky ID, Liu Z, Wei H, Fernando HJS (2008b) Tides and mixing in the northwestern East China Sea Part II: Near-bottom turbulence. Cont Shelf Res 28:338–350.

Lu Y, Lueck RG (1999) Using a broadband ADCP in a tidal channel Part II: Turbulence. J Atmos Oceanic Tech 16:1568–1579.

Ludwick JC (1975) Variations in the boundary-drag coefficient in the tidal entrance to Chesapeake Bay, Virginia. Mar Geol 19:19–28.

Lueck RG, Mudge TD (1997) Topographically induced mixing around a shallow seamount. Science 276:1831–1833.

Lueck RG, Lu Y (1997) The logarithmic layer in a tidal channel. Cont Shelf Res 17:1785–1801.

MacKinnon JA, Gregg MC (2003) Mixing on the late-summer New England Shelf – solibores, shear and stratification. J Phys Oceanogr 33:1476–1492.

Matsuno T, Lee JS, Shimizu M, Kim SH, Pang IC (2006) Measurements of the turbulent energy dissipation rate ε and an evaluation of the dispersion process of the Changjiang Diluted Water in the East China Sea. J Geophys Res 111:C11S09. doi:10.1029/2005JC003196.

Merrifield MA, Holloway PE (2002) Model estimates of M_2 internal tide energetics at the Hawaiian Ridge. J Geophys Res 107: 3179. doi:10.1029/2001JC00996.

Mohn C, Beckmann A (2002) The upper ocean circulation at Great Meteor Seamount. Part I:

Structure of density and flow fields. Ocean Dyn 52:179–193.

Moum JN, Caldwell DR, Nash JD, Gunderson GD (2002) Observations of boundary mixing over the continental slope. J Phys Oceanogr 32:2113–2130.

Moum JN, Perlin A, Klymak JM, Levine MD, Boyd T, Kosro PM (2004) Convectively driven mixing in the bottom boundary layer. J Phys Oceanogr 34:2189–2202.

Mueller, DS Abad JD, García CM, Gartner JW, García MH, Oberg KA (2007) Errors in acoustic Doppler profiler velocity measurements caused by flow disturbance J Hydr Engrg 133(12): 1411-1420.

Muste M, Dongsu K., González-Castro JA (2010) Near-transducer errors in ADCP measurements: experimental findings J Hydr Engrg 136(5): 275-289.

Niwa Y, Hibiya T (2004) Three-dimensional numerical simulation of M_2 internal tides in the East China Sea. J Geophys Res 109:C04027. doi:10.1029/2003JC001923.

Nabatov VN, Ozmidov RV (1988) A study of turbulence over underwater mountains in the Atlantic Ocean. Oceanology 28:210– 217 (in Russian).

Oakey NS (1982) Determination of the rate of dissipation of turbulent energy from simultaneous temperature and velocity shear microstructure measurements. J Phys Oceanogr 12:256–271.

Paka VT, Nabatov VN, Lozovatsky ID, Dillon TM (1999) Oceanic microstructure measurements by “Baklan” and “Grif”. J Atmos Oceanic Tech 16:1519–1532.

Palmer MR, Rippeth TP, Simpson JH (2008) An investigation of internal mixing in a seasonally stratified shelf sea. J Geophys Res 113: C12005. doi:10.1029/2007JC004531.

Perlin A, Moum JN, Klymak JM, Levine MD, Boyd T, Kosro PM (2005) A modified

law-of-the-wall applied to oceanic bottom boundary layers. J Geophys Res 110:C10S10. doi:10.1029/2004JC002310.

Prandke H, Stips A (1998) Test measurements with an operational microstructure-turbulence profiler: Detection limits of dissipation rates. Aquat Sci 60:191–209.

Rippeth TP, Inall ME (2002) Observations of the internal tide and associated mixing across the Malin Shelf. J Geophys Res 107:3028. doi:10.1029/2000JC000761.

Roget E, Lozovatsky I, Sanchez X, Figueroa M (2006) Microstructure measurements in natural waters: Methodology and applications. Prog Oceanogr 70:123–148.

Sanford TB, Lien RC (1999) Turbulent properties in a homogeneous tidal bottom boundary layer. J Geophys Res 104:1245–1257. doi:10.1029/1998JC900068.

Schauer U (1987) Determination of bottom boundary layer parameters at two shallow sea sites using the profile method. Cont Shelf Res 7:1211–1230.

Sherwin TJ, Vlasenko VI, Stashchuk N, Jeans DRG, Jones B (2002) Along-slope generation as an explanation for some unusually large internal tides. Deep-Sea Res I 49:1787–1799.

Soulsby R. 1980 Selecting record length and digitization rate for near-bed turbulence measurements. J. Phys. Oceanogr 10(2):208-219.

Simpson JH, Crawford WR, Rippeth TP, Campbell AR, Cheok JVS (1996) The vertical structure of turbulent dissipation in shelf seas. J Phys Oceanogr 26:1579–1590.

Smith JD, McLean SR (1977) Spatially averaged flow over a wavy surface. J Geophys Res 82:1735–1746.

Stacey MT, Monismith SG, Burau JR (1999) Measurements of Reynolds stress profiles in tidal

flows. J Geophys Res 104:10933–10949.

Taylor JR, Sarkar S (2008) Stratification effects in a bottom Ekman layer. J Phys Oceanogr 38:2535–2555.

Thorpe SA (2005) The turbulent ocean. Cambridge University Press, Cambridge, UK.

Weatherly GL, Martin PJ (1978) On the dynamics and structure of the oceanic bottom boundary layer. J Phys Oceanogr 8:557–570.

Wolk F, Yamazaki H, Seuront L, Lueck RG (2002) A new free-fall profiler for measuring biophysical microstructure. J Atmos Oceanic Tech 19:780–793.

Xu Y, Fernando HJS, Boyer DL (1995) Turbulent wake of stratified flow passed a cylinder. Phys Fluids 7:2243–2255.

Zilitinkevich SS, Esau I (2002) On integral measures of the neutral barotropic planetary boundary layers. Bound-Layer Meteorol 104:371–379.

Figure Captions

Fig. 1. The measurement site (circled snowflake) and surrounding bathymetry. The double-head arrow represents the radius of a bathymetric rise, which is about 2.5 – 3 km between 25 and 35 m isobaths. The distance from the rise to the site is shown by a single-head arrow.

Fig. 2. (a) The surface elevation ξ_{BT} of barotropic tide (OTIS calculation) at the test site [the period of microstructure measurements is thickened and the pressure gauge data are shown by diamonds]. (b) The 10-min running averaged time series of zonal u and meridianal v current components at various heights ζ above the seafloor. (c) The clockwise rotating ADCP current ellipses at same heights as in (b) with 1 hr time step (left and lower axes) and the OTIS barotropic tidal ellipse (right and upper axes). Time in hours from the beginning of ADCP measurements [0, 3, 6, 9, 12, 15, 18] is depicted for ζ = 0.4 mab (magenta) and for the OTIS ellipses.

Fig. 3. (a) Time-depth variation of the logarithm of the dissipation rate ε (color palette) overlaid by contours of specific potential density σ_θ. Splitting of the main pycnocline is highlighted by the rectangle between t = 14 and 23 hrs and z > 14 m.

(b) Temperature and salinity at isopycnal surfaces below the near-surface sharp thermocline (σ_θ > 21, z > ~ 8 – 11 m); an approximate central position of the pycnocline splitting is marked by a dashed line (σ_θ = 23) corresponding to the depth range ~ 21 – 23 m.

Fig. 4. Temperature (a) and salinity (b) profiles obtained during the first 18 hrs of measurements (hourly casts started at 9:00 Sep 3, 2006); max(h_B) and min(h_B) are the estimated maximum and minimum heights of a weakly-stratified BBL in all 18 profiles.

Fig. 5. Examples of the 10-min averaged near-bottom ADCP velocity profiles $U(\zeta)$. The profiles are shown with a 3-hr time interval; two additional profiles (at 7 and 17 hrs) are added for a phase of very weak western upslope flow. The least squared fits to the logarithmic model are shown by continuous lines.

Fig. 6. The cumulative distribution functions CDF(r^2) of the coefficient of determination r^2 for the logarithmic fit to the velocity profiles $U(\zeta)$ in the range ζ = 0.04 – 0.48 mab for averaging with different time scales τ (note that $r^2 < 0.5$ for only 1% of the 5-min averaged profiles).

Fig. 7. The friction velocities u_* obtained via logarithmic fits to the velocity profiles $U_\tau(\zeta)$ averaged with different time scales τ (a), and the drag coefficient $C_D = u_*^2 / U^2_{(1\,\mathrm{m})}$ for non-overlapping 10-min segments (b).

Fig. 8. The MMS dissipation profiles $\varepsilon_{mc}(\zeta)$ and the law-of-the-wall profiles $\varepsilon_{wl}(\zeta)$ for (a) along-slope southward flow, (b) along-slope northward flow, (c) across-slope eastward flow, and (d) across-slope westward flow (τ = 30 and 10 min).

Fig. 9. The magnitude of the internal tide generating body force F near and to the east of the test site (P11) in the background of a local bathymetry (the isobaths -30, …, - 60 are marked in meters). The black curves encircle the areas with $F > 0.25$ m^2/s^2.

Fig. 10. The dissipation rate ($log_{10}\,\varepsilon$) west of the Baker Island (a) and to the southwest of the summit of seamount Castor (b). The upper 100-m layer in (a) was occupied by a turbulent zone of the Equatorial Surface Current. The shaded region in (a) and the area bounded by

dashed lines in (b) are the turbulent zones selected for calculating the respective averaged dissipations $\bar{\varepsilon}(x)$.

Fig. 11. The averaged dissipation rate $\bar{\varepsilon}(x)$ at a distance x downstream from the summits of the designated seamounts and islands. The inverse distance dependences $\bar{\varepsilon} = u_o^3 x^{-1}$ are shown for three characteristic velocity scales u_o (straight and dashed lines) that span variability of external forcing; the values of u_o are indicated.

Fig. 12. The averaged dissipation rate $\tilde{\varepsilon}(x/D)$ west of the Baker Island; x/D the normalized distance westward of the island and D = 2.6 km the island diameter in the depth range 50 – 80 m.

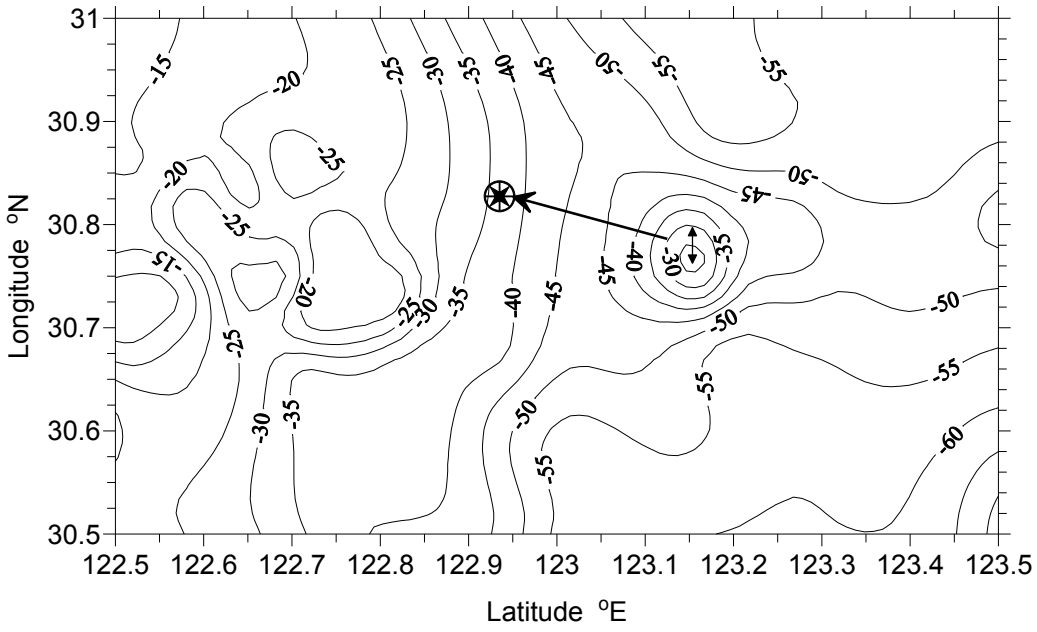

Fig.1. The measurement site (circled snowflake) and surrounding bathymetry. The double-head arrow represents the radius of a bathymetric rise, which is about 2.5 – 3 km between 25 and 35 m isobaths. The distance from the rise to the site is shown by a single-head arrow.

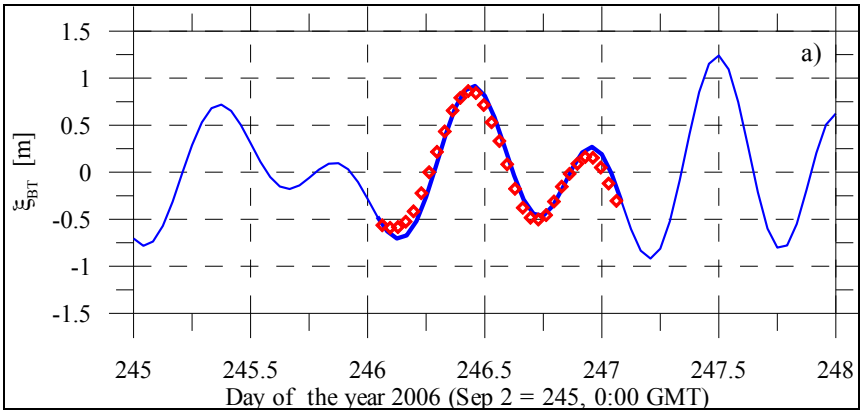
a)
ξ_{BT} [m]
1.5
1
0.5
0
-0.5
-1
-1.5
245
245.5
246
246.5
247
247.5
248
Day of the year 2006 (Sep 2 = 245, 0:00 GMT)

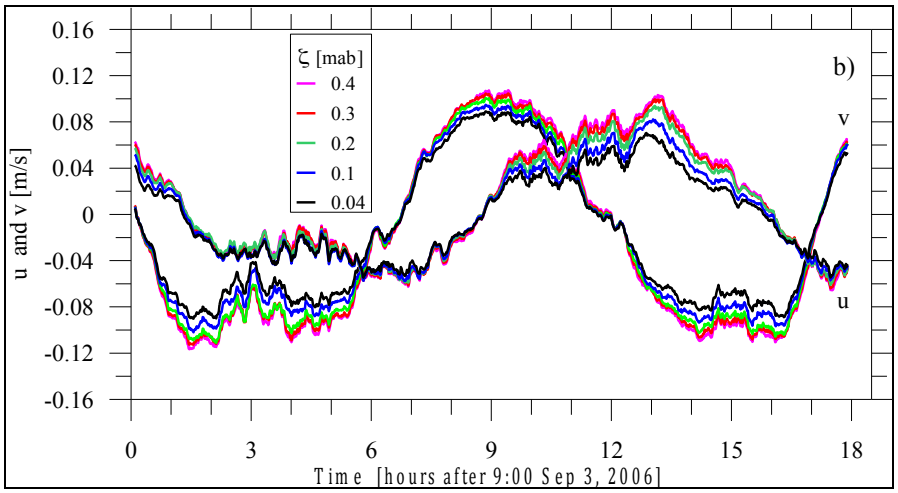
b)
ζ [mab]
0.4
0.3
0.2
0.1
0.04
v
u
u and v [m/s]
0.16
0.12
0.08
0.04
0
-0.04
-0.08
-0.12
-0.16
0
3
6
9
12
15
18
Time [hours after 9:00 Sep 3, 2006]

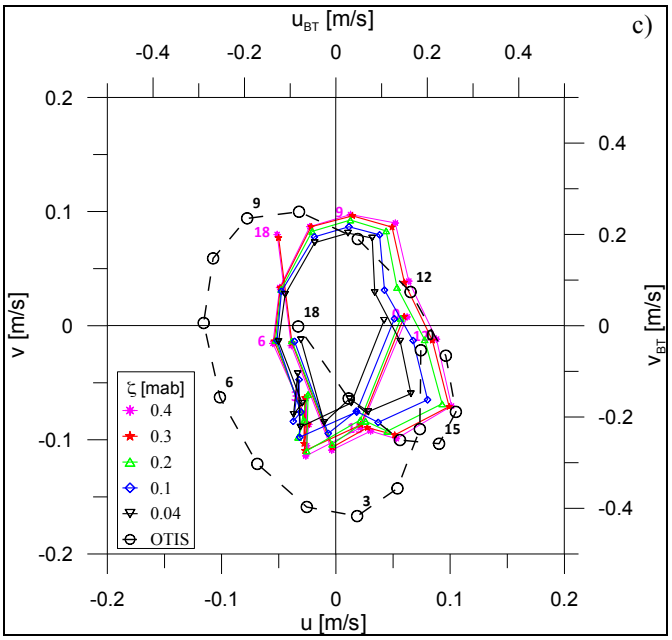
c)
u_{BT} [m/s]
-0.4
-0.2
0
0.2
0.4
v [m/s]
v_{BT} [m/s]
u [m/s]
ζ [mab]
0.4
0.3
0.2
0.1
0.04
OTIS

Fig.2. (a) The surface elevation ξ_{BT} of barotropic tide (OTIS calculation) at the test site [the period of microstructure measurements is thickened and the pressure gauge data are shown by diamonds]. (b) The 10-min running averaged time series of zonal u and meridianal v current components at various heights ζ above the seafloor. (c) The clockwise rotating ADCP current ellipses at same heights as in (b) with 1 hr time step (left and lower axes) and the OTIS barotropic tidal ellipse (right and upper axes). Time in hours from the beginning of ADCP measurements [0, 3, 6, 9, 12, 15, 18] is depicted for ζ = 0.4 mab (magenta) and for the OTIS ellipses.

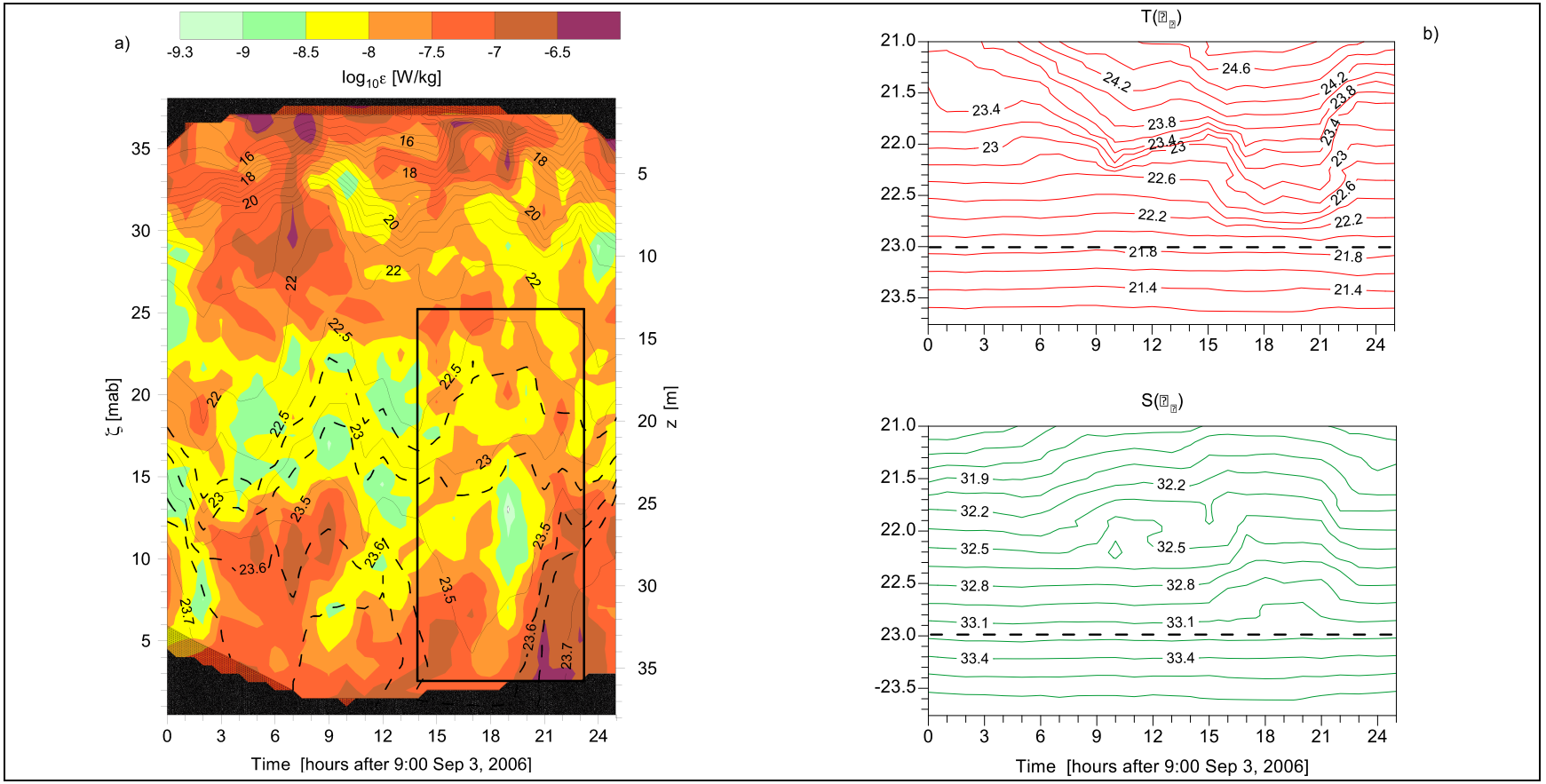

Fig.3. (a) Time-depth variation of the logarithm of the dissipation rate ε (color palette) overlaid by contours of specific potential density σ_θ. Splitting of the main pycnocline is highlighted by the rectangle between t = 14 and 23 hrs and z > 14 m.

(b) Temperature and salinity at isopycnal surfaces below the near-surface sharp thermocline (σ_θ > 21, z > ~ 8 – 11 m); an approximate central position of the pycnocline splitting is marked by a dashed line (σ_θ = 23) corresponding to the depth range ~ 21 – 23 m.

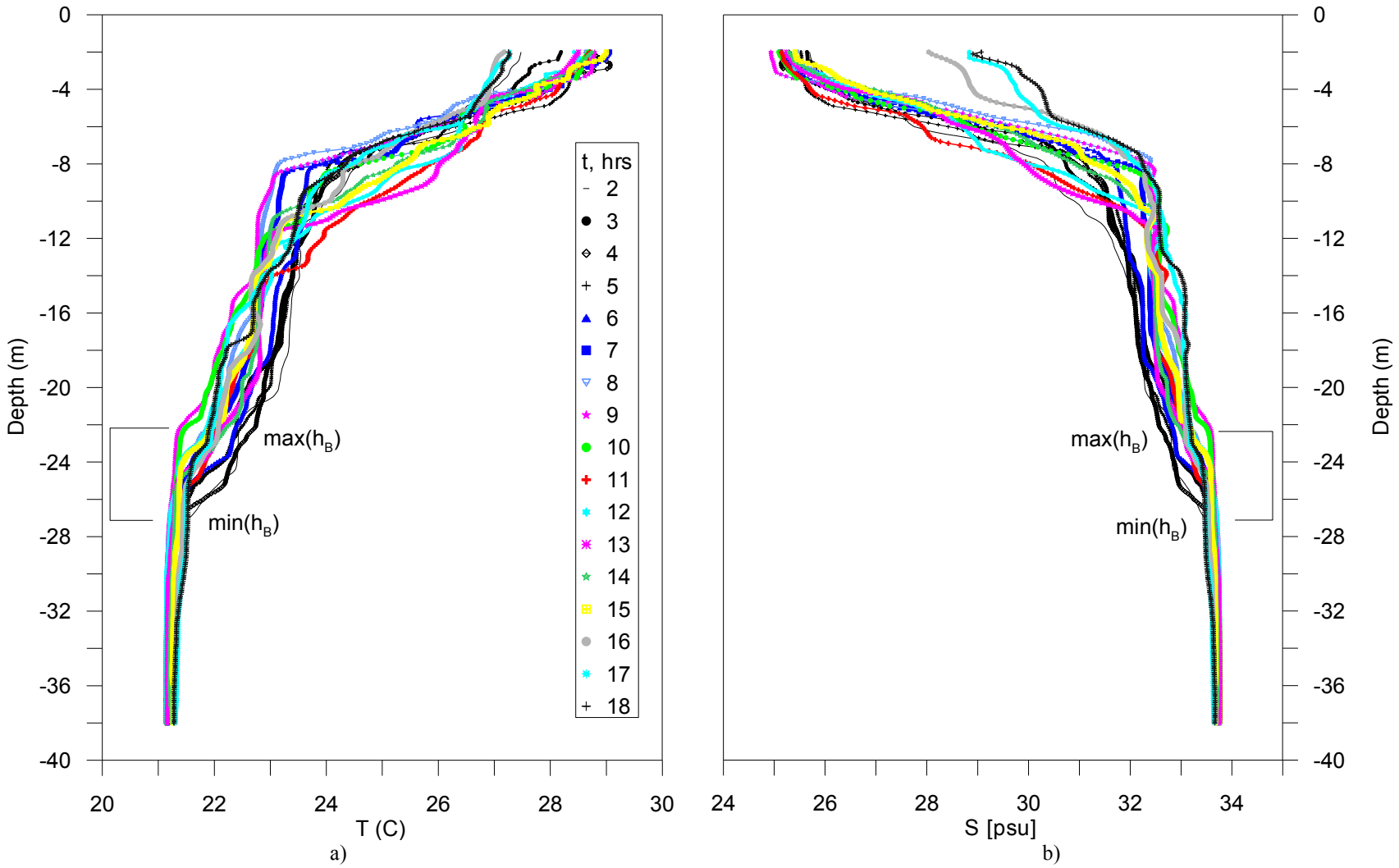

Fig.4. Temperature (a) and salinity (b) profiles obtained during the first 18 hrs of measurements (hourly casts started at 9:00 Sep 3, 2006); max(h_B) and min(h_B) are the estimated maximum and minimum heights of a weakly-stratified BBL in all 18 profiles.

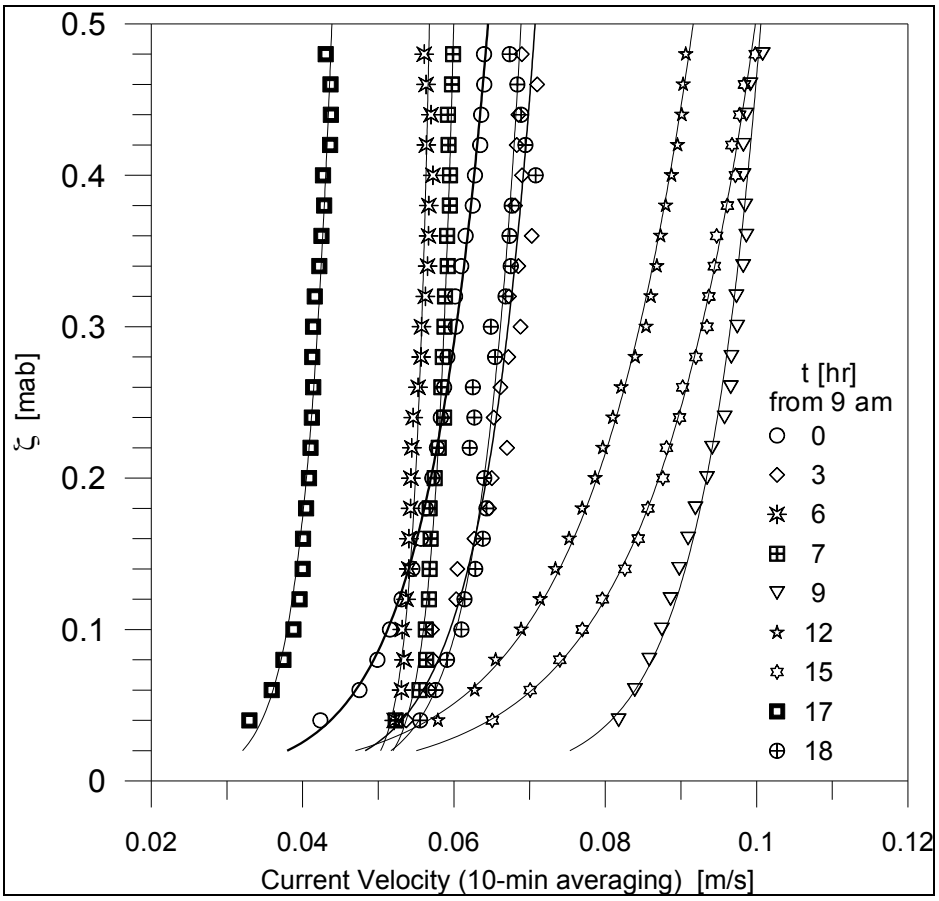

Fig.5. Examples of the 10-min averaged near-bottom ADCP velocity profiles $U(\zeta)$. The profiles are shown with a 3-hr time interval; two additional profiles (at 7 and 17 hrs) are added for a phase of very weak western upslope flow. The least squared fits to the logarithmic model are shown by continuous lines.

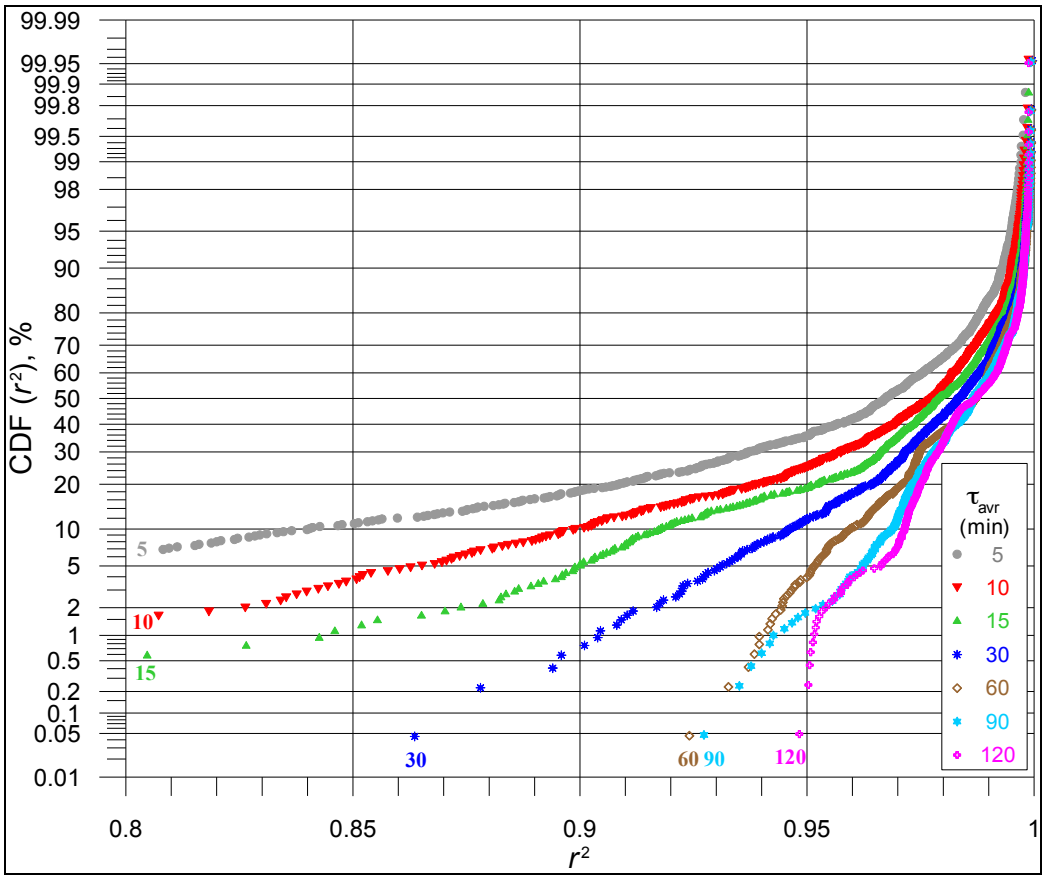

Fig.6. The cumulative distribution functions CDF(r^2) of the coefficient of determination r^2 for the logarithmic fit to the velocity profiles $U(\zeta)$ in the range ζ = 0.04 – 0.48 mab for averaging with different time scales τ (note that $r^2 < 0.5$ for only 1% of the 5-min averaged profiles).

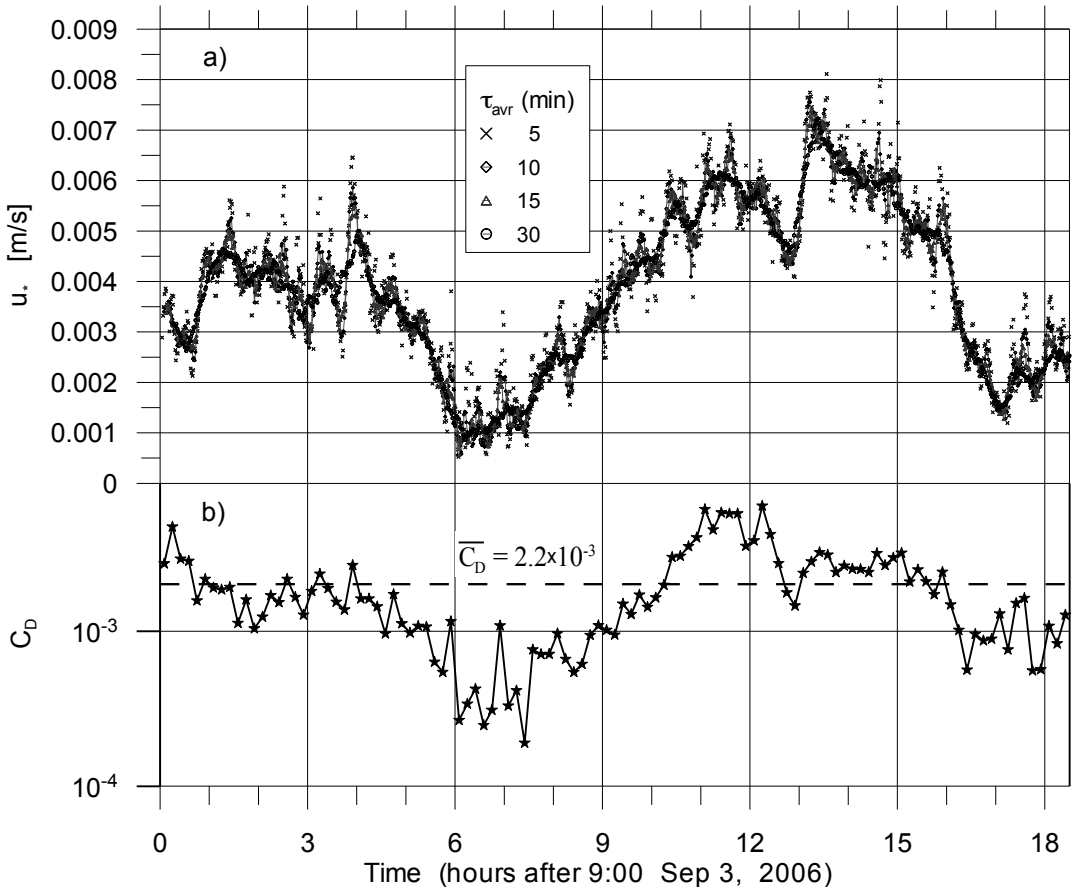

Fig.7. The friction velocities u_* obtained via logarithmic fits to the velocity profiles $U_\tau(\zeta)$ averaged with different time scales τ (a), and the drag coefficient $C_D = u_*^2 / U^2_{(1\,\mathrm{m})}$ for non-overlapping 10-min segments (b).

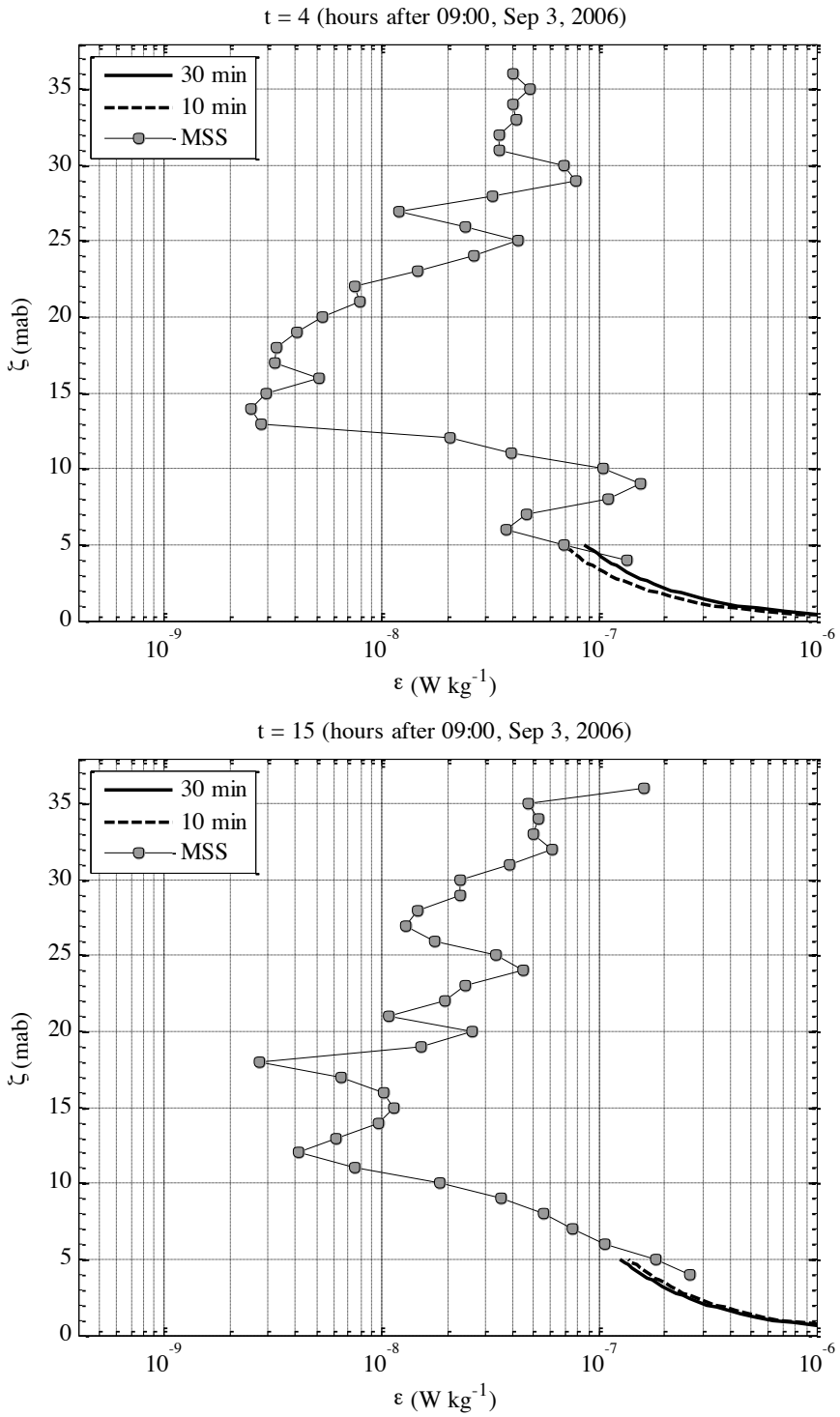

Fig.8a. The MSS $\varepsilon_{mc}(\zeta)$ and the law-of-the-wall $\varepsilon_{wl}(\zeta)$ dissipation profiles for along-slope southward flow (τ = 30 and 10 min).

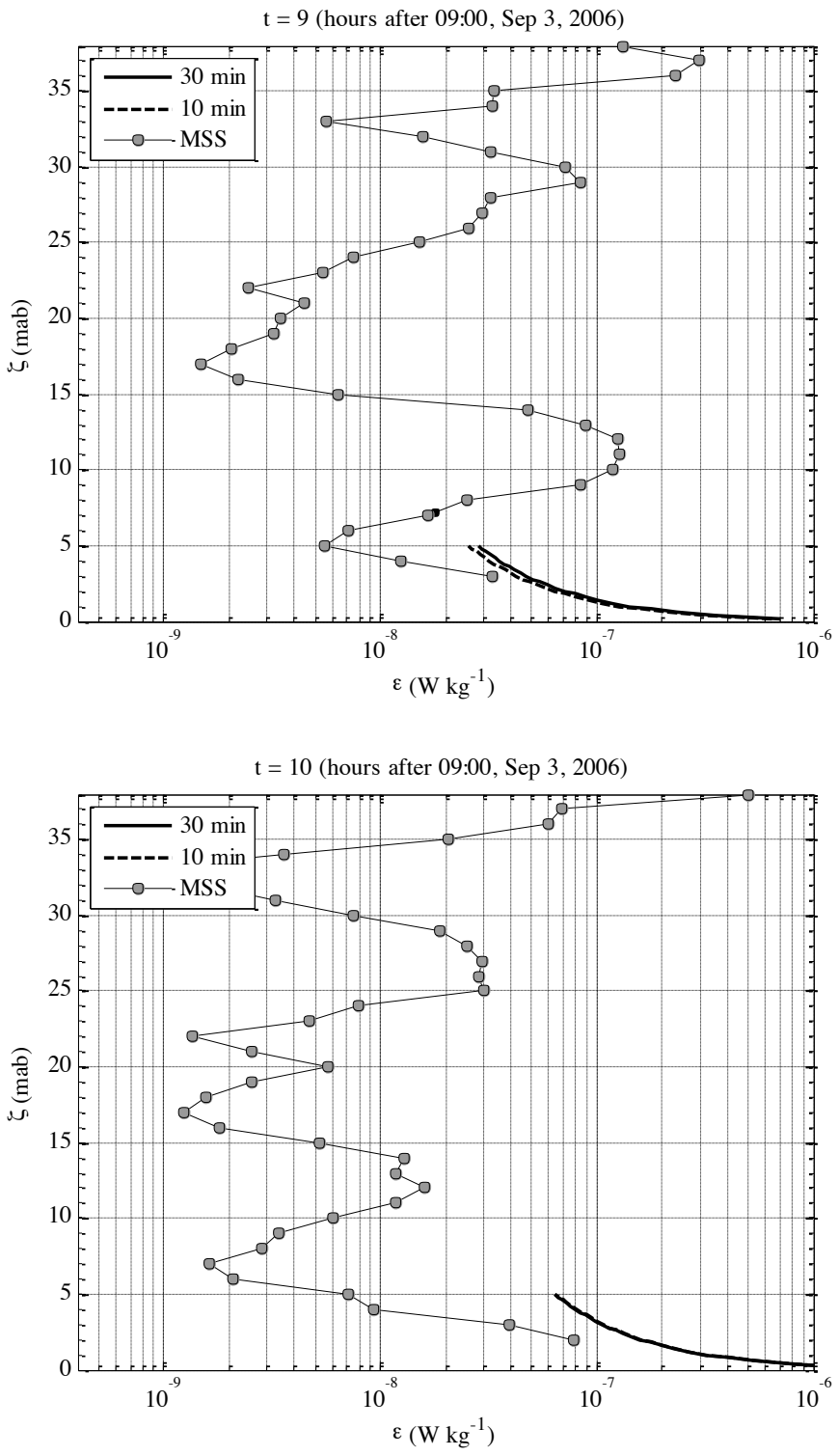

Fig.8b. The MSS $\varepsilon_{mc}(\zeta)$ and the law-of-the-wall $\varepsilon_{wl}(\zeta)$ dissipation profiles for along-slope northward flow.

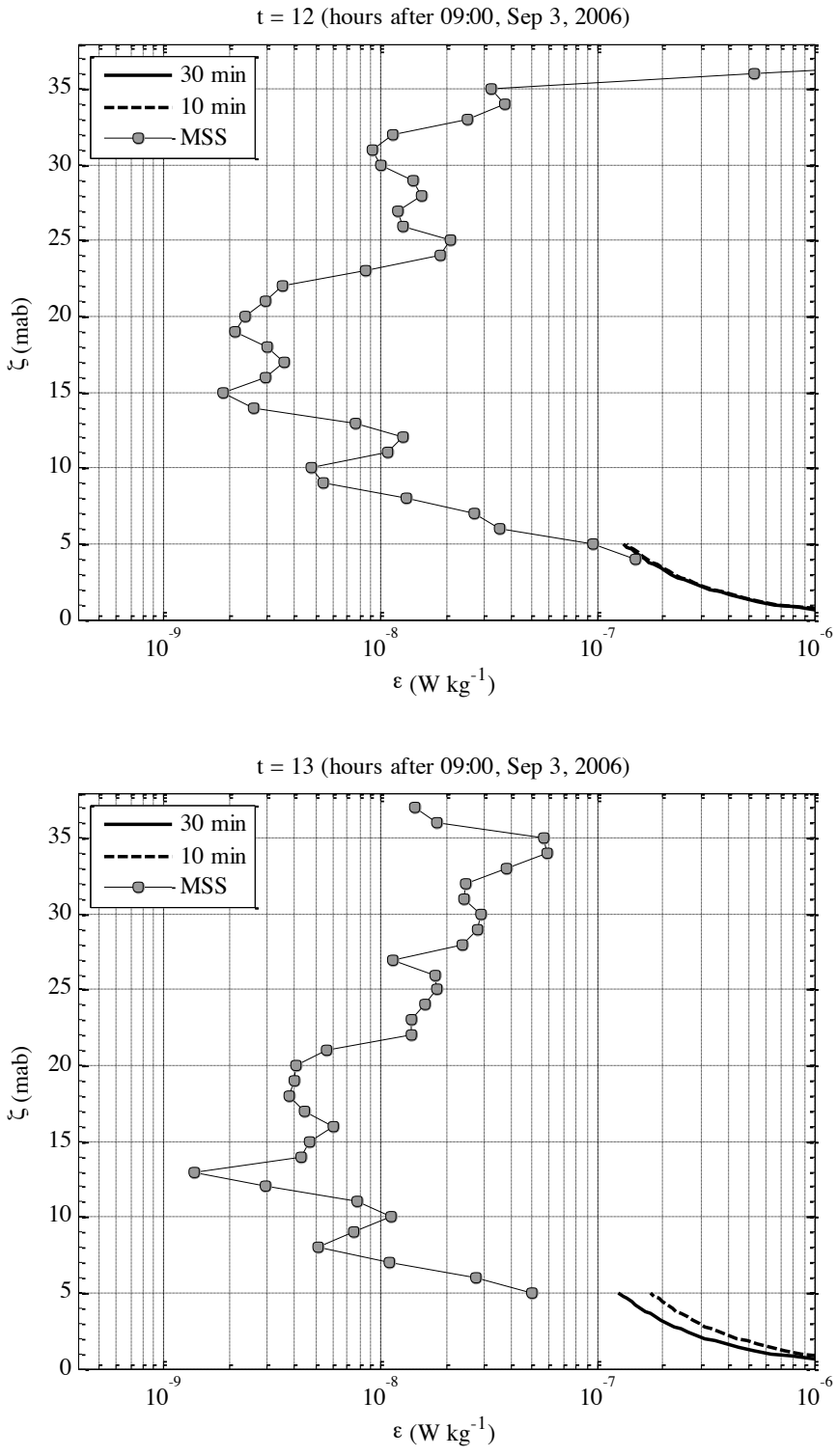

Fig.8c. The MSS $\varepsilon_{mc}(\zeta)$ and the law-of-the-wall $\varepsilon_{wl}(\zeta)$ dissipation profiles for across-slope eastward flow.

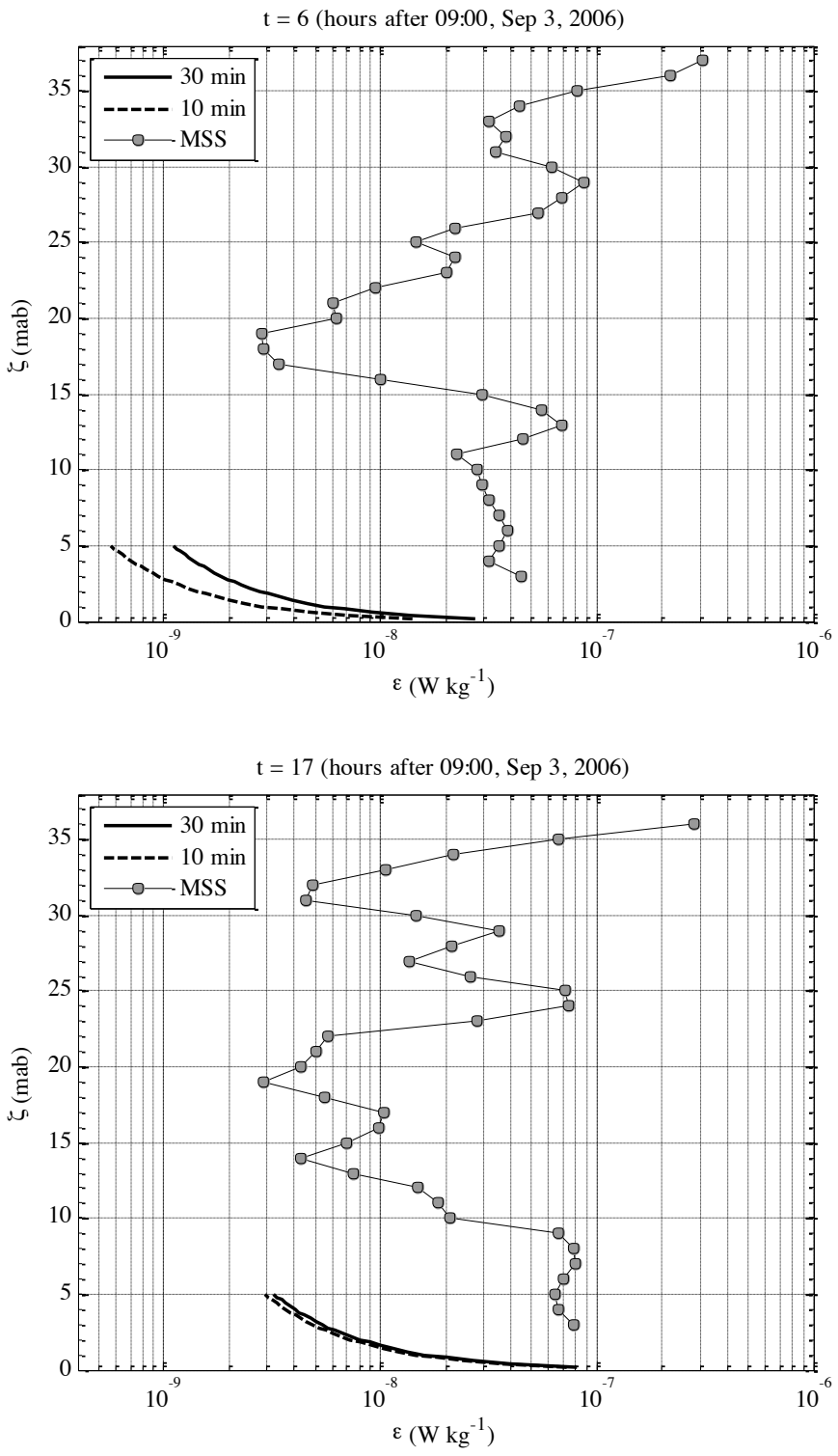

Fig.8d. The MSS $\varepsilon_{mc}(\zeta)$ and the law-of-the-wall $\varepsilon_{wl}(\zeta)$ dissipation profiles for across-slope westward flow.

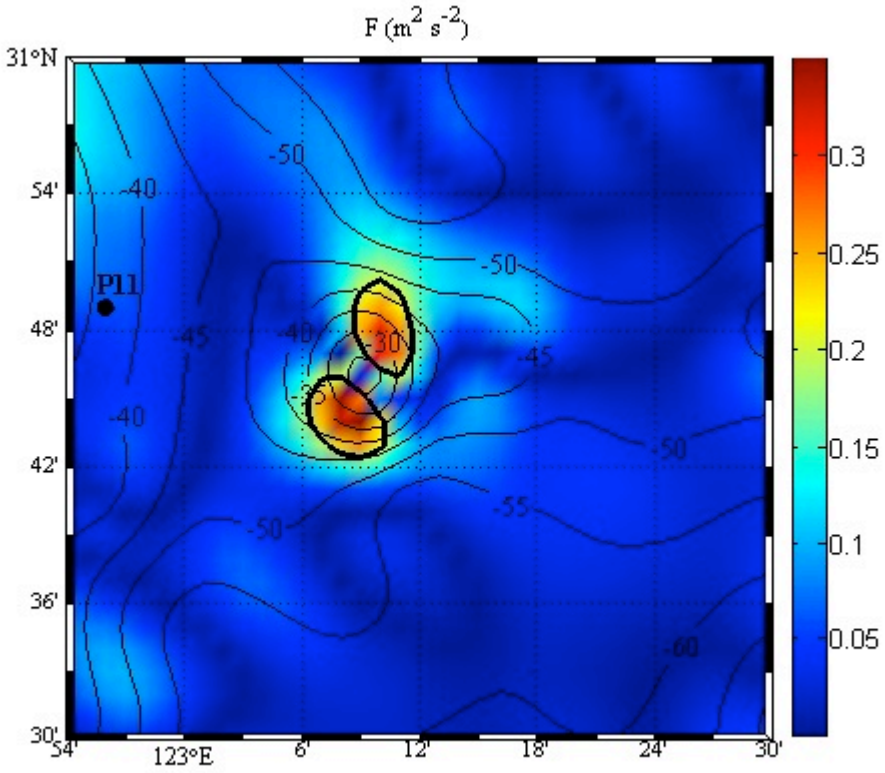

Fig.9. The magnitude of the internal tide generating body force F near and to the east of the test site (P11) in the background of a local bathymetry (the isobaths -30, …, - 60 are marked in meters). The black curves encircle the areas with $F > 0.25$ m^2/s^2.

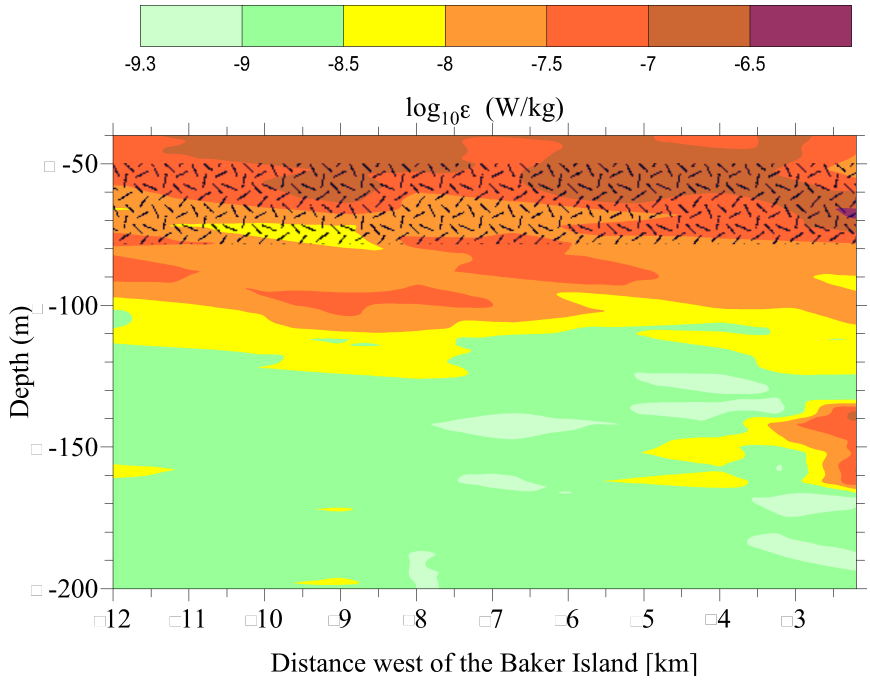

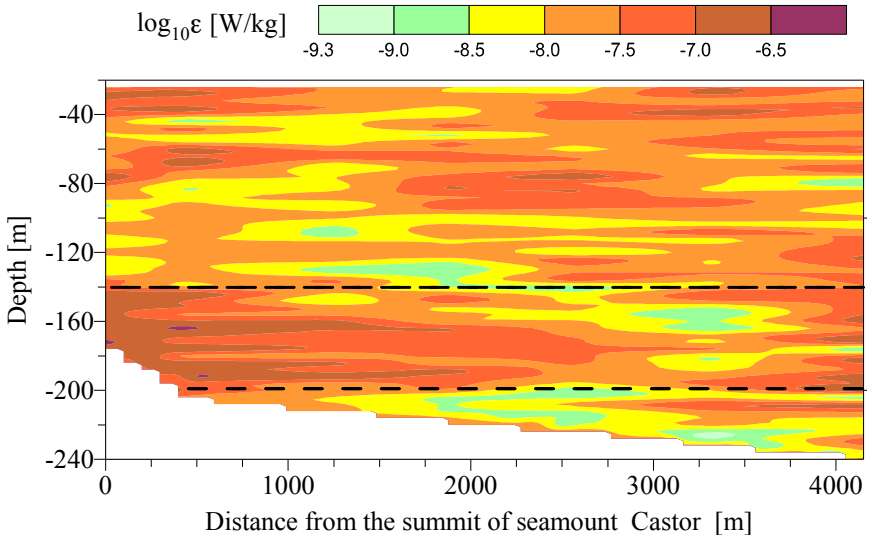

Fig.10. The dissipation rate ($log_{10}\,\varepsilon$) west of the Baker Island (a) and to the southwest of the summit of seamount Castor (b). The upper 100-m layer in (a) was occupied by a turbulent zone of the Equatorial Surface Current. The shaded region in (a) and the area bounded by dashed lines in (b) are the turbulent zones selected for calculating the respective averaged dissipations $\bar{\varepsilon}(x)$.

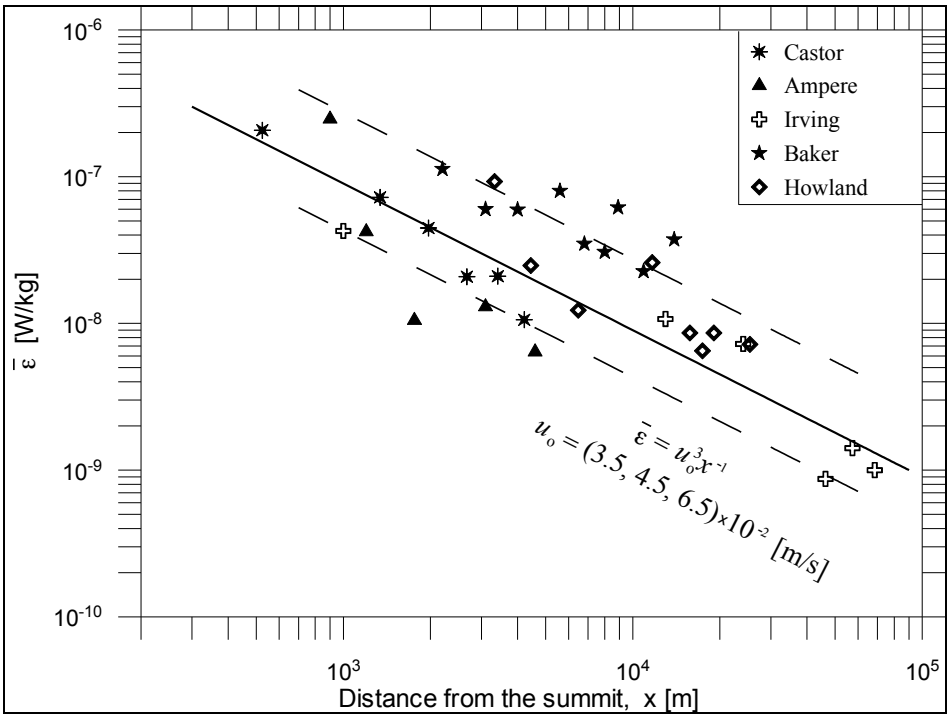

Fig.11. The averaged dissipation rate $\bar{\varepsilon}(x)$ at a distance *x* downstream from the summits of the designated seamounts and islands. The inverse distance dependences $\bar{\varepsilon} = u_o^3 x^{-1}$ are shown for three characteristic velocity scales u_o (straight and dashed lines) that span variability of external forcing; the values of u_o are indicated.

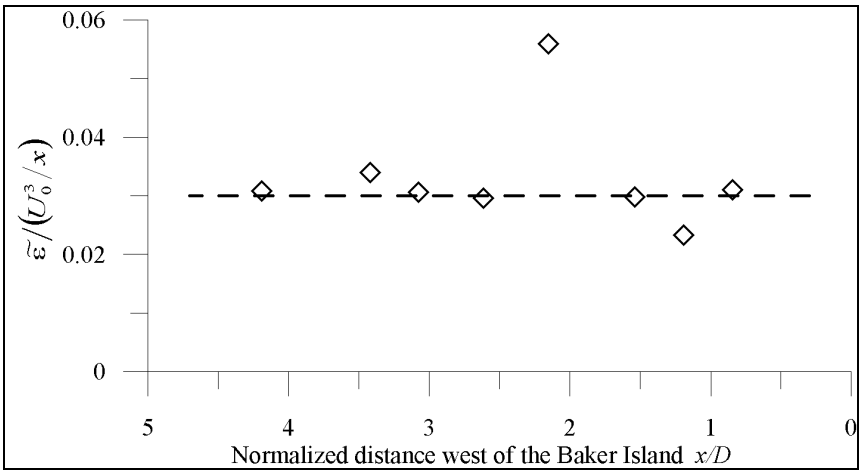

Fig.12. The averaged dissipation rate $\tilde{\varepsilon}(x/D)$ in the wake of the Baker Island; x/D the normalized distance westward of the island and D = 2.6 km the island diameter in the depth range 50 – 80 m.

Table 1. Values of the turbulent zone Froude Fr_{tz} and Reynolds Re_{tz} numbers and the ratio h_{tz}/D, where h_{tz} is a thickness of the turbulent zone at a distance *x* behind an obstacle (seamount or island) of diameter *D*.

Topography	$Fr_{tz} = U_0/N_0 h_{tz}$	$Re_{tz} = U_0 D/\nu$	h_{tz}/D
Baker Island	0.83	5.2×10^{8}	1.2×10^{-2}
Present case	0.91 – 1.36	$(1.2-1.8)\times10^{9}$	1.7×10^{-3}

Response to Reviewers' Comments

Two minor corrections have been made, as kindly pointed out by the two reviewers. We greatly appreciate the two reviewers for their critical reviews and very helpful comments. We thank the Editor, Dr. Alex Souza for his editorial work!

Lozovatsky, Liu, Fernando, Armengol, and Roget